Chemistry–A European Journal

Supporting Information

# Water Sorption Controls Extreme Single-Crystal-to-Single-Crystal Molecular Reorganization in Hydrogen Bonded Organic Frameworks

Stephanie A. Boer, Luke Conte, Andrew Tarzia, Michael T. Huxley, Michael G. Gardiner, Dominique R. T. Appadoo, Courtney Ennis, Christian J. Doonan, Christopher Richardson,* and Nicholas G. White*

# Synthesis and characterization

## *General remarks*

NMR spectra were collected on a Bruker Avance spectrometer and are referenced to the residual solvent signal.[1] Thermogravimetric analyses were recorded on a TA Instruments Q500 analyser under flowing nitrogen. Simultaneous thermal gravimetric and differential scanning calorimetry (TG-DSC) data were recorded from 30 °C to 600 °C using a Netzsch STA449F3 SiC furnace at 4°C $min^{-1}$ under a flow of $N_2$ or 5% $O_2$ in $N_2$ at 20 mL $min^{-1}$. TG-DSC analysis was conducted using Netzsch Proteus-Thermal analysis-version 6.1.0. TG-DSC data for water vapour isotherms were collected under isothermal conditions of 40 °C using the Netzsch STA449F3 Cu furnace equipped with a modular humidity generator attachment (ProUmid GmbH & Co. KG, MHG32) and mixer module in conjunction with an external, adjustable temperature zone controller. The humidity was controlled following a programmed experiment designed on MHG32 software, and a humidified nitrogen gas flow of 150 $cm^3$ $min^{-1}$. Samples of approximately 5–6 mg were placed into concavus aluminium pans without lids. Samples of the γ-phase were generated by heating the α-phase to 130 °C under $N_2$ at 20 mL $min^{-1}$ before starting the program at low humidity. Equilibration times for points were evaluated in line with the DSC response; once the signal reached a baseline value, the next RH % value was collected. PXRD data were recorded using a PANalytical Empyrean diffractometer using Cu Kα radiation and a PIXcel detector. SCXRD data were recorded on either a SuperNova diffractometer or at the Australian Synchrotron; further details are provided in the SCXRD section of this document.

## *Synthesis of tectons*

**Carbon-centred tectons:** We have made improvements to the synthesis of various compounds over the course of this work. We have attempted to optimize the syntheses of previously reported compounds to give reasonable quantities of material in decent yield and without tedious purification (Scheme S1). These materials were prepared from tetra(bromophenyl)methane (**S1**), which was prepared by brominating tetraphenylmethane, as described.[2] Tetraphenylmethane is commercially available (although is relatively expensive USD ~$20/g)[3] or can be prepared in two steps from trityl chloride.[2]

**Silicon-centred tectons:** These were prepared following literature procedures without modification.[4,5]

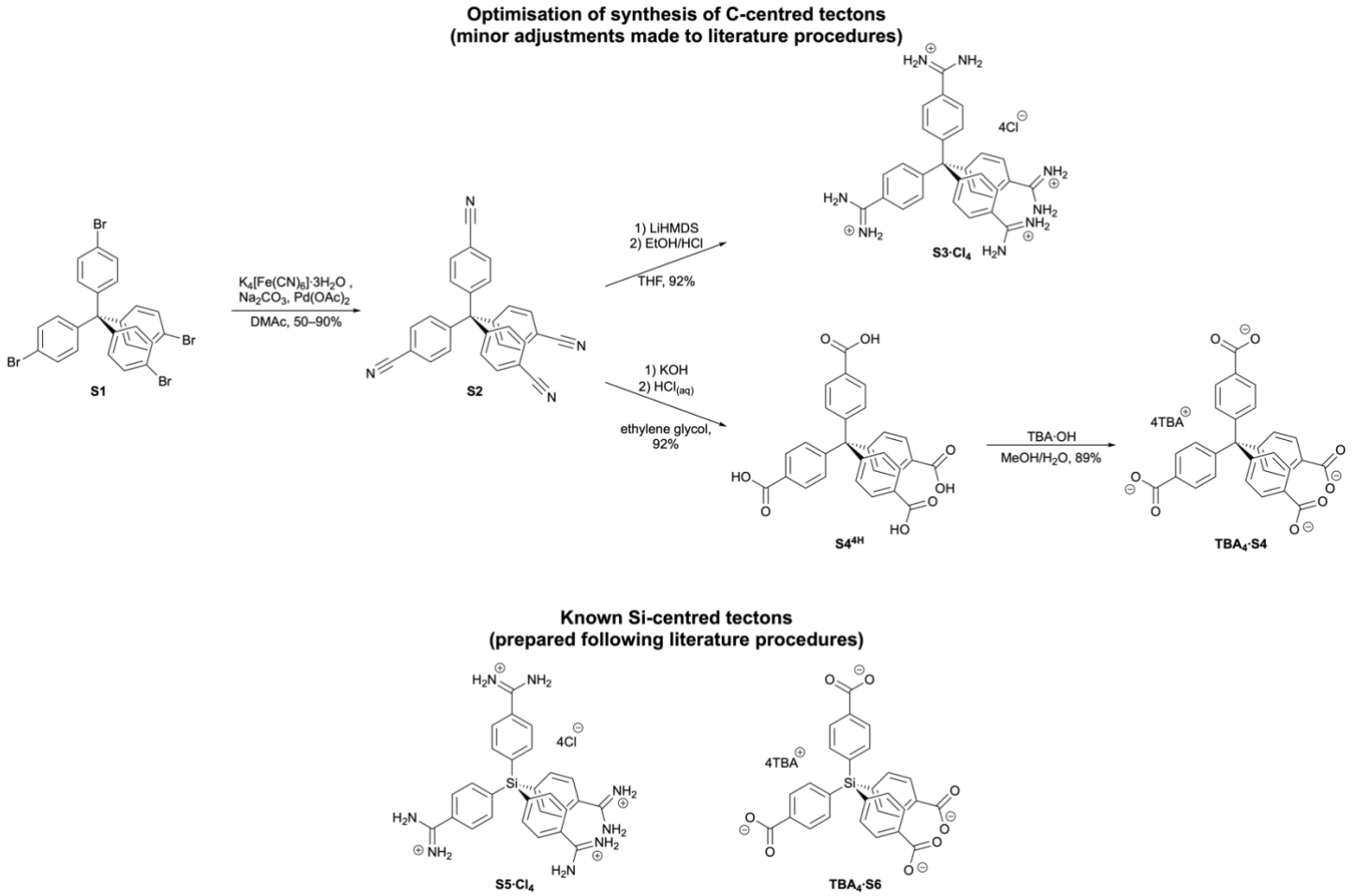


**Scheme S1.** Optimised syntheses of carbon-centred tectons and structure of silicon-centred tectons.

**Tetranitrile S2:** *Prepared by a modification of our previously-reported procedure.*[6]

We reported that this compound could be prepared from tetrabromo compound **S2** in 89% yield with purification by simple precipitation.[6] Repeating this reaction has shown that it is somewhat variable: the yield of tetranitrile is sometimes essentially quantitative, while at other times crude product yields are less good (80–90% based on $^1$H NMR analysis of the crude reaction mixture) with an organic impurity present. We have not been able to find recrystallization conditions suitable for bulk purification and so purify this compound by careful column chromatography (the impurity tends to co-elute with the product if the column is eluted too quickly). Even when the reaction goes "badly," we are still able to obtain 50–60% yields of pure isolated product after column chromatography. If the reaction goes well and essentially quantitative conversion is observed, then it can be purified by precipitation in good yield (80–90%) as described.[6] Unfortunately, we have not been able to determine what influences the variability of this reaction.

*A procedure for a reaction where quantitative conversion to the tetranitrile was not observed follows:* Compound **S1** (1.91 g, 3.00 mmol), $Na_2CO_3$ (1.59 g, 15.0 mmol), $K_4[Fe(CN)_6{\cdot}3H_2O$ (2.53 g, 6.00 mmol) and $Pd(OAc)_2$ (0.034 g, 0.15 mmol) were placed in a round-bottomed flask containing a large stirrer bar. Dimethylacetamide (12 mL) was added and the pale suspension heated to 120 °C overnight under a nitrogen atmosphere. The brown colored solution was cooled to room temperature, diluted with ethyl acetate (60 mL), and filtered through a short pad of Celite, washing through with further ethyl acetate (2 × 20 mL). The combined organic phases were washed with $NH_{3(aq)}$ (5%, 50 mL), water (50 mL) and brine (50 mL), then dried ($MgSO_4$) and taken to dryness under reduced pressure to give a pale brown foam. Column chromatography (150 mL $SiO_2$ as the stationary phase, $CH_2Cl_2$ as eluent) gave **S2** as a white powder. Yield: 0.755 g (1.80 mmol, 60%).

Spectral data were consistent with those previously reported;[6] the $^1$H NMR spectrum is shown in Figure S1.

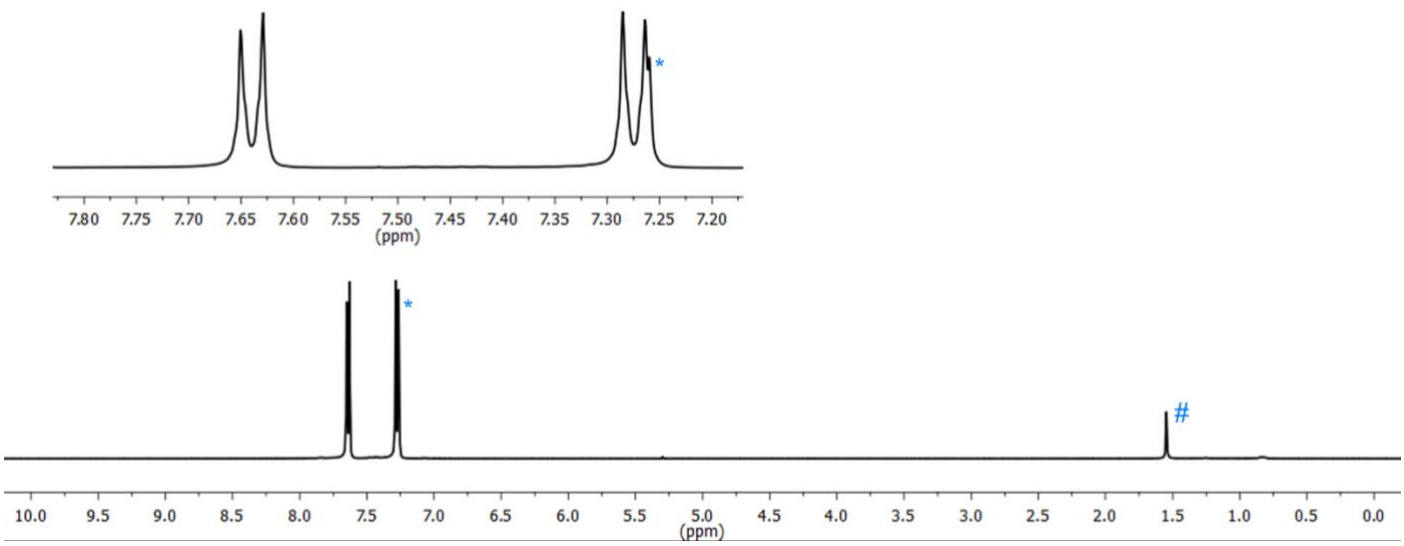


**Figure S1.** $^1$H NMR spectrum of tetranitrile **S2**; peak marked # is due to water, peak marked * is due to the NMR solvent ($CDCl_3$, 400 MHz, 298 K). Peaks are not integrated due to the overlap of one of the two peaks with the NMR solvent signal.

**Tetra-amidinium S3·Cl$_4$:** *Prepared by a modification of our previously-reported procedure.*[7]

Tetranitrile **S2** (0.420 g, 1.00 mmol) was suspended in THF (10 mL) and cooled in an ice-bath under a nitrogen atmosphere. A solution of LiHMDS in THF (1.0 M, 6.0 mL, 6.0 mmol) was added slowly, causing the white suspension to turn to a clear golden solution. The ice-bath was removed, and the solution was stirred at room temperature under a nitrogen atmosphere overnight. Separately, ethanol (18 mL) was cooled in an ice-bath, and with vigorous stirring acetyl chloride (2 mL) was added cautiously to give a solution of ethanolic HCl. The THF reaction mixture was cooled in an ice-bath, and the ethanolic HCl mixture added slowly resulting in the formation of a pale precipitate. The ice-bath was removed and the mixture stirred at room temperature for 1 hour. The precipitate was isolated by filtration, and washed with EtOH (3 × 10 mL). The white powder was then suspended in EtOH (50 mL), sonicated for 1 hour, and the powder again isolated by filtration, washed with EtOH (3 × 10 mL) and then dried thoroughly *in vacuo*. Yield: 0.583 g (0.919 mmol, 92%).

*Note: the $^1$H NMR spectrum of **S3·Cl$_4$** after the first filtration (before the EtOH sonication step) is consistent with tetraamidinium salt contaminated with NH$_4$Cl. This re-suspension and sonication procedure removes this. It is also possible that LiCl could be present, but given LiCl has far higher solubility in EtOH than NH$_4$Cl, we assume that once all NH$_4$Cl has been removed, the LiCl has also gone.*

Spectral data were consistent with those previously reported;[7] the $^1$H NMR spectrum is shown in Figure S2.

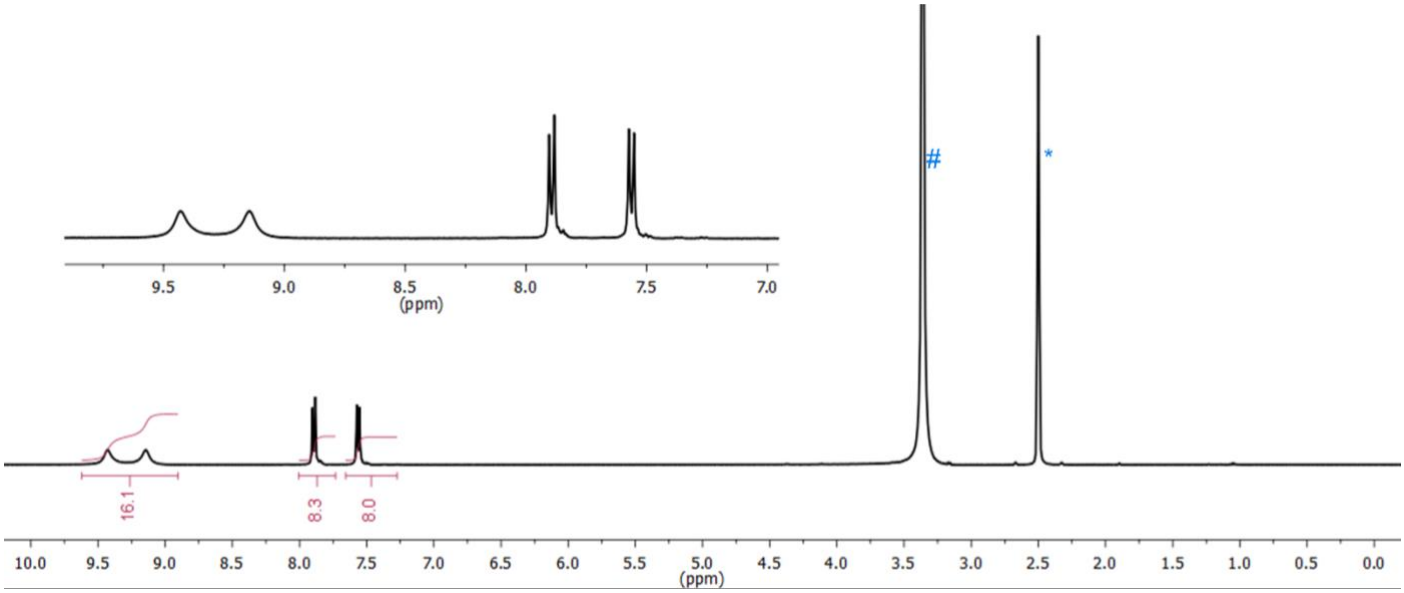


**Figure S2.** $^1$H NMR spectrum of tetraamidinium **S3·Cl$_4$**; peak marked # is due to water, peak marked * is due to the NMR solvent signal (d$_6$-DMSO, 400 MHz, 298 K).

**Tetra-acid S4$^{4H}$:** *Prepared by a modification of the procedure reported by Kurreck and colleagues.*[8]

Tetranitrile **S2** (0.420 g, 1.00 mmol) and KOH pellets (1.12 g, 20.0 mmol) were suspended in ethylene glycol (20 mL), and the white suspension heated to 180 °C under a nitrogen atmosphere overnight. Upon heating all material dissolved to give a yellow-brown solution. The reaction was cooled to room temperature and $HCl_{(aq)}$ (1.0 M, 60 mL, 60 mmol) was added resulting in the precipitation of a white powder. This was isolated by filtration, washed with $H_2O$ (3 × 10 mL), then MeOH (3 × 5 mL), and dried *in vacuo*. Yield: 0.457 g (0.920 mmol, 92%).

Spectral data were consistent with those previously reported;[9] the $^1$H NMR spectrum is shown in Figure S3.

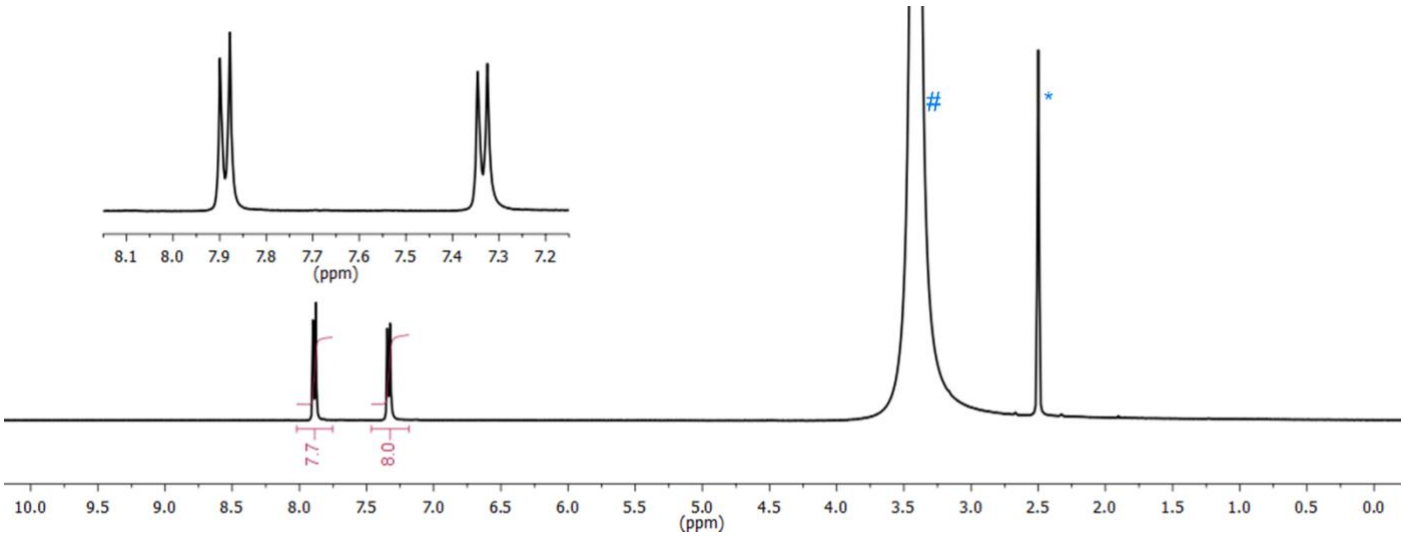


**Figure S3.** $^1$H NMR spectrum of tetracarboxylic acid **S4$^{4H}$**; peak marked # is due to water, peak marked * is due to the NMR solvent signal ($d_6$-DMSO, 400 MHz, 298 K).

**Tetra-carboxylate $TBA_4$·S4:** *Prepared by a modification of our previously-reported procedure.*[10]

Tetracarboxylic acid **$S4^{4H}$** (0.397 g, 0.800 mmol) was suspended in $H_2O$ (20 mL). A solution of TBA·OH in methanol (1.0 M, 3.2 mL, 3.2 mmol) was added and the mixture stirred for 10 minutes during which time all material dissolved (if any large chunks of the acid are present, it may be necessary to break these up using a stirring rod to aid dissolution). The pale brown solution was then taken to dryness *in vacuo*. The resulting pale brown powder was taken up in hot acetone (15 mL) and allowed to cool to room temperature. Diethyl ether (15 mL) was added resulting in the formation of a white powder. This was isolated by filtration, washed with 1:1 acetone:diethyl ether (2 × 5 mL) and dried *in vacuo* to give 0.870 g (0.595 mmol, 74%) of a white powder. The combined filtrates were evaporated to dryness and taken up in hot acetone (10 mL); after cooling to room temperature, diethyl ether (20 mL) was added resulting in the precipitation of a white powder. This was isolated by filtration, washed with 1:2 acetone:diethyl ether (2 × 5 mL) and dried *in vacuo*. Yield of this crop: 0.172 g (0.118 mmol, 15%). NMR spectroscopy showed that both crops were pure product. Combined yield: 1.04 g (0.712 mmol, 89%).

*Note: $^1H$ and $^{13}C$ NMR spectroscopy indicate that the crude powder obtained before the precipitation step is relatively pure product and in our earlier studies we used this "crude" material to prepare hydrogen bonded frameworks.*[10] *However, due to the possibility of minor inaccuracies in measuring out the reagents it is probable that this crude product either contains small amounts of incompletely deprotonated material, or of excess TBA·OH. Given the ease of the purification step and the potential for any residual hydroxide to degrade the amidinium groups,*[11] *we now use this precipitation step when preparing* ***$TBA_4$·S4****.*

Spectral data were consistent with those previously reported,[10] the $^1H$ NMR spectrum of the first crop is shown in Figure S4 and of the second crop is shown in Figure S5.

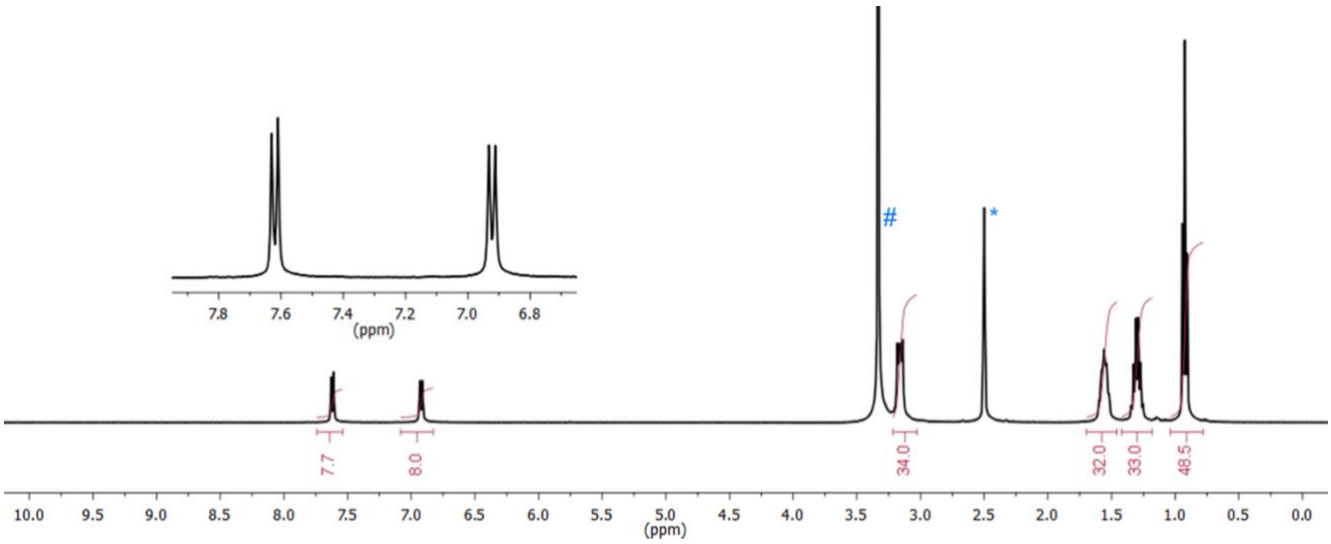


**Figure S4.** $^{1}$H NMR spectrum of first crop of **TBA$_4$·S4**; peak marked # is due to water, peak marked * is due to the NMR solvent signal (d$_6$-DMSO, 400 MHz, 298 K).

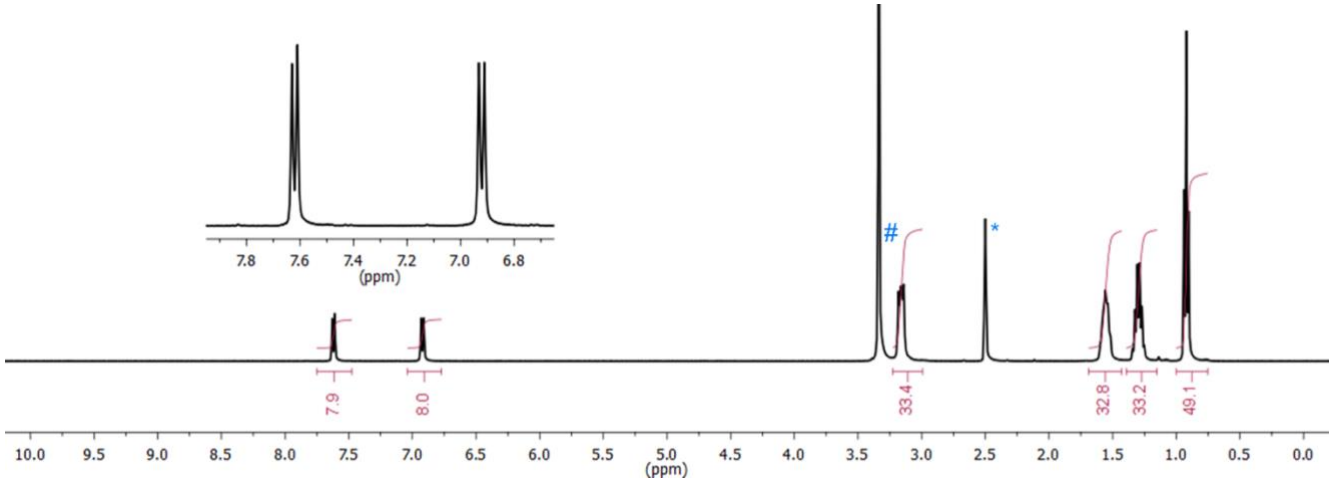


**Figure S5.** $^{1}$H NMR spectrum of second crop of **TBA$_4$·S4**; peak marked # is due to water, peak marked * is due to the NMR solvent signal (d$_6$-DMSO, 400 MHz, 298 K).

## *Synthesis of hydrogen bonded frameworks*

**α-1$^{C/C}$:** *We have reported the synthesis of this framework on a 61 mg scale.*[10] *Given that we studied this material extensively in this work, we have optimized the synthesis on a larger scale.*

A solution of **TBA$_4$·S4** (0.292 g, 0.200 mmol) in EtOH (50 mL) was added to a solution of **S3·Cl$_4$** (0.127 g, 0.200 mmol) in water (50 mL) resulting in the immediate formation of a white precipitate. The mixture was left to stand at room temperature overnight, then the precipitate was isolated by filtration, washed with water (3 × 10 mL), then EtOH (3 × 10 mL) and air-dried to give **α-1$^{C/C}$** as a white powder. Yield: 0.222 g (0.185 mmol, 92%).

Yield calculated based on 12 water molecules per formula unit, as indicated by SCXRD, EA and TGA.

Spectral data were consistent with those previously reported;[9] the $^1$H NMR spectrum of acid-digested framework is shown in Figure S6.

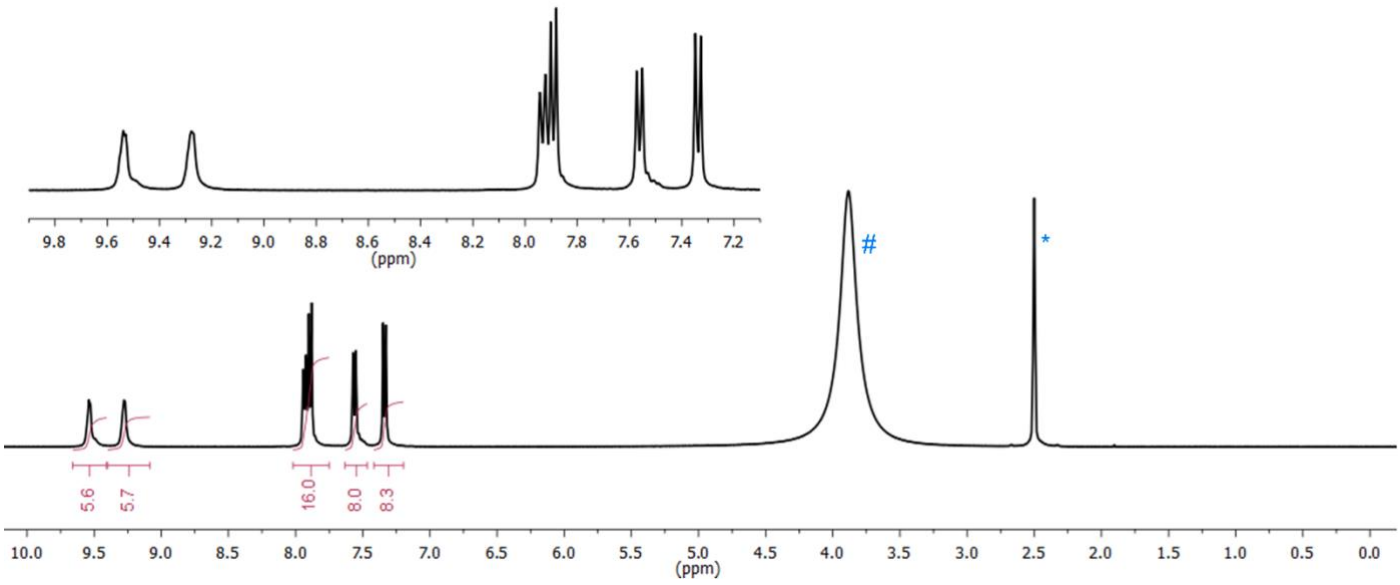


**Figure S6.** $^1$H NMR spectrum of **1$^{C/C}$**; peak marked # is due to water, peak marked * is due to the NMR solvent signal. The integration of the amidinium N–H resonances is lower than expected, which we attribute to H/D exchange ($d_6$-DMSO containing a drop of 20% DCl in $D_2O$, 400 MHz, 298 K).

**α-1$^{Si/C}$:** *This was prepared as described.*[4]

**α-1$^{Si/Si}$:** *This was prepared as described*.[5]

# SCXRD

## *Data collection and refinement*

**Data collection:** Data for **α-1$^{C/C}$** at 100 and 273 K, and **β-1$^{C/C}$** were collected on the MX2 beamline[12] at the Australian Synchrotron. Data for **α-1$^{C/C}$** at 313 K were collected on the MX1 beamline[13] at the Australian Synchrotron. Raw frame data for synchrotron data (including data reduction, interframe scaling and unit cell refinement) were processed using XDS.[14]

Data for **α-1$^{C/C}$** at 150 K, **γ-1$^{C/C}$**, **triclinic-1$^{Si/C}$** and **triclinic-1$^{Si/Si}$** were collected using mirror-monochromated Cu Kα radiation on an Agilent SuperNova diffractometer at 150 K. Raw frame data (including data reduction, interframe scaling, unit cell refinement and absorption corrections) were processed using CrysAlis Pro.[15]

**Data refinement:** The structures of **α-1$^{C/C}$** at 100 and 273 K, **β-1$^{C/C}$**, **triclinic-1$^{Si/C}$** and **triclinic-1$^{Si/Si}$** were solved using Superflip,[16] the structures of **α-1$^{C/C}$** at 150 K and 313 K, and **γ-1$^{C/C}$** were solved using SHELXT.[17] All structures were refined using full-matrix least-squares on $F^2$ within the Crystals suite.[18] All non-hydrogen atoms were refined with anisotropic displacement parameters. Unless otherwise stated, C–H hydrogen atoms were generally visible in the Fourier difference map, and were initially refined with restraints on bond lengths and angles, after which the positions were used as the basis for a riding model.[19]

Full crystallographic data in CIF format are provided as Supporting Information (CCDC Numbers: 2169825–2169832). Selected data are summarised in Table S1, and the individual structures are discussed in more detail in the following section.

**Table S1.** Selected crystallographic data.

| Compound | α-1$^{C/C}$ at 100 K | α-1$^{C/C}$ at 150 K | α-1$^{C/C}$ at 273 K | α-1$^{C/C}$ at 313 K |
|---|---|---|---|---|
| Radiation type | synchrotron (λ = 0.71073 Å) | Cu Kα (λ = 1.54184 Å) | synchrotron (λ = 0.71073 Å) | synchrotron (λ = 0.71073 Å) |
| Temperature (K) | 100 | 150 | 273 | 313 |
| Formula | $C_{29}H_{32}N_8 \cdot C_{29}H_{16}O_8 \cdot (H_2O)_{12}$ | $C_{29}H_{32}N_8 \cdot C_{29}H_{16}O_8 \cdot (H_2O)_{12}$ | $C_{29}H_{32}N_8 \cdot C_{29}H_{16}O_8 \cdot (H_2O)_{12}$ | $C_{29}H_{32}N_8 \cdot C_{29}H_{16}O_8 \cdot (H_2O)_{12}$ |
| Formula weight | 1201.25 | 1201.25 | 1201.25 | 1201.25 |
| *a* (Å) | 20.357(2) | 20.336(3) | 20.437(3) | 20.462(3) |
| *b* (Å) | 20.357(2) | 20.336(3) | 20.437(3) | 20.462(3) |
| *c* (Å) | 15.647(2) | 15.672(3) | 15.626(3) | 15.617(3) |
| $\alpha$ (º) | 90 | 90 | 90 | 90 |
| *β* (º) | 90 | 90 | 90 | 90 |
| *γ* (º) | 90 | 90 | 90 | 90 |
| Unit cell volume (Å$^3$) | 6484.49(4) | 6481.3(2) | 6526(2) | 6539(2) |
| Crystal system | tetragonal | tetragonal | tetragonal | tetragonal |
| Space group | $I4_1/a$ | $I4_1/a$ | $I4_1/a$ | $I4_1/a$ |
| *Z* | 4 | 4 | 4 | 4 |
| Reflections (all) | 41766 | 6453 | 60167 | 30310 |
| Reflections (unique) | 3216 | 2813 | 5160 | 2339 |
| $R_{int}$ | 0.089 | 0.024 | 0.119 | 0.070 |
| $R_1$ [$I > 2\sigma(I)$] | 0.055 | 0.047 | 0.066 | 0.074 |
| $wR_2$ (all data) | 0.175 | 0.131 | 0.220 | 0.233 |
| CCDC number | 2169825 | 2169826 | 2169827 | 2169828 |

| Compound | β-1$^{C/C}$ | γ-1$^{C/C}$ | triclinic-1$^{Si/C}$ [a] | triclinic-1$^{Si/Si}$ [a] |
|---|---|---|---|---|
| Radiation type | synchrotron (λ = 0.71073 Å) | Cu Kα (λ = 1.54184 Å) | Cu Kα (λ = 1.54184 Å) | Cu Kα (λ = 1.54184 Å) |
| Temperature (K) | 100 | 318 | 150 | 150 |
| Formula | $(C_{29}H_{32}N_8)_{0.5} \cdot (C_{29}H_{16}O_8)_{0.5} \cdot 4H_2O$ | $C_{29}H_{32}N_8 \cdot C_{29}H_{16}O_8$ | $C_{28}H_{32}N_8Si \cdot C_{29}H_{16}O_8 \cdot$*solvents*[a] | $C_{28}H_{32}N_8Si \cdot C_{28}H_{16}O_8Si \cdot$*solvents*[a] |
| Formula weight | 564.59 | 985.07 | 1001.14 | 1017.22 |
| *a* (Å) | 12.981(2) | 17.923(3) | 14.4524(4) | 14.6188(3) |
| *b* (Å) | 12.981(2) | 17.923(3) | 16.9609(3) | 17.8113(5) |
| *c* (Å) | 16.430 (3) | 15.500(4) | 17.8904(5) | 18.2903(4) |
| $\alpha$ (º) | 90 | 90 | 83.084(2) | 87.944(2) |
| *β* (º) | 90 | 90 | 67.145(3) | 67.461(2) |
| *γ* (º) | 90 | 90 | 70.867(2) | 66.172(2) |
| Unit cell volume (Å$^3$) | 2768.6(9) | 4979(2) | 3817.75(19) | 3983.64(19) |
| Crystal system | tetragonal | tetragonal | triclinic | triclinic |
| Space group | $P4_3$ | *I*–4 | *P*–1 | *P*–1 |
| *Z* | 4 | 4 | 2 | 2 |
| Reflections (all) | 25038 | 4103 | 59246 | 65455 |
| Reflections (unique) | 2076 | 2531 | 15328 | 15980 |
| $R_{int}$ | 0.178 | 0.113 | 0.032 | 0.039 |
| $R_1$ [$I > 2\sigma(I)$] | 0.110 | 0.109 | 0.060 | 0.049 |
| $wR_2$ (all data) | 0.193 | 0.289 | 0.182 | 0.144 |
| CCDC number | 2169829 | 2169830 | 2169831 | 2169832 |

[a] PLATON SQUEEZE used.[20]

## *Variable temperature SCXRD*

**α to β phase transition:** If crystals of **α-1$^{C/C}$** are heated to approximately 323 K on a goniometer pin, the long needle-like crystals droop and bend (Figure S7) causing a massive reduction in crystallinity. Using microfocus synchrotron radiation, it was possible to index a part of one of these drooped crystals, which gave a unit cell consistent with **β-1$^{C/C}$**, however it was not possible to obtain data that would allow us to solve the crystal structure.

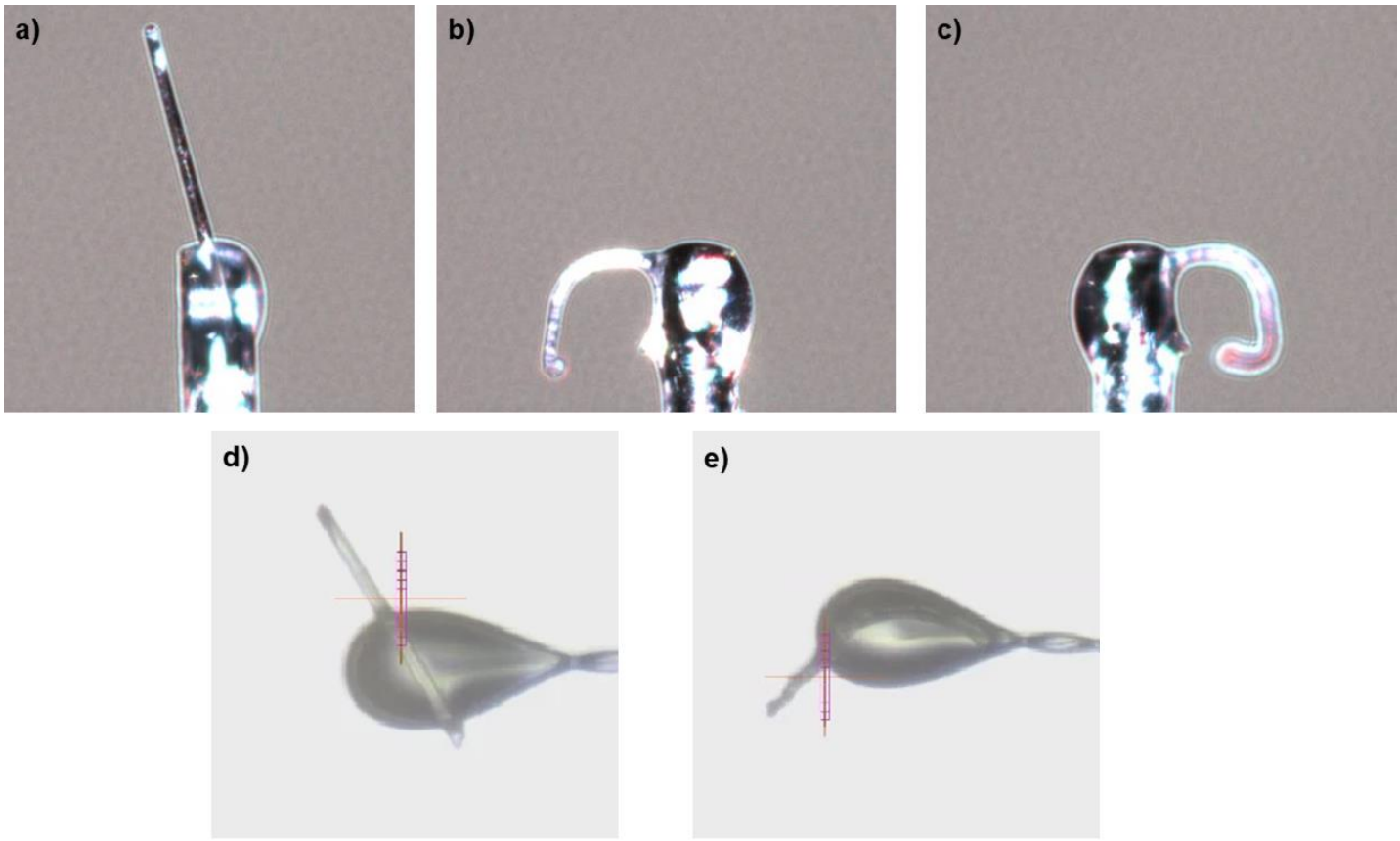


**Figure S7.** Pictures of drooping of single crystals of **α-1$^{C/C}$** upon heating. Pictures a–c are of the same crystal (approx. dimensions: 0.50 × 0.02 × 0.02 mm) glued to a goniometer pin on a home-source diffractometer before heating (a) and after heating to 323 K (b and c). Pictures d and e are of the same crystal (approx. dimensions: 0.25 × 0.02 × 0.02 mm) in oil on a loop at the Australian Synchrotron before heating (d) and after heating to 323 K (e).

Rather than heating crystals individually on a pin, crystals were deposited on a glass microscope slide. This slide was heated on a hotplate at 338 K for 10 minutes. During this process, a few crystals jumped off the slide, but most bent slightly. Presumably this slight bending instead of the drastic drooping when the crystal was mounted on a goniometer pin is due to the support provided by the flat glass slide. These crystals were of reduced quality compared to the unheated crystals, but could be used for synchrotron SCXRD experiments, which revealed that they were **β-1$^{C/C}$**. Collecting unit cell data at either room temperature, 173 K or 100 K were consistent with the β-phase, *i.e.* no reversion to the α-phase was observed upon cooling.

**β to γ phase transition:** TGA and PXRD experiments reveal that the β to γ transition occurs at approximately 363 K. Variable temperature SCXRD experiments were conducted using synchrotron radiation: crystals of **β-1$^{C/C}$** were mounted on a loop and data collected at 280, 300, 320, 340, 360 and 380 K ramping at 6 K min$^{-1}$ between collections. Under these conditions, a phase change was observed at 340 K giving unit cell parameters consistent with **γ-1$^{C/C}$**, although crystallinity deteriorated significantly so the structure could not be solved. When a crystal of **β-1$^{C/C}$** was mounted on a home-source diffractometer and collected at 318 K over approximately 24 hours, the initial screening gave a unit cell consistent with **β-1$^{C/C}$** but the final dataset refined as the γ-phase. Presumably the warm dry nitrogen stream used to warm the sample was sufficient to remove the water from the sample.

## *Structures of α-1$^{C/C}$ at 100, 150, 273 K and 313 K*

We have collected structures of **α-1$^{C/C}$** at several different temperatures. Note that not all of the structures were recorded on the same crystal. We have collected several datasets on each of several crystals at various temperatures using synchrotron radiation but found the crystals suffered radiation damage over time resulting in reduced data quality. In this section we report our highest quality refinements for various temperatures. However, we note that all refined structures of **α-1$^{C/C}$** show exactly the same arrangements of amidinium and carboxylate tectons, as well as well-ordered water molecules in all cases.

**Structure of α-1$^{C/C}$ at 100 K:** We have previously reported the structure of **α-1$^{C/C}$** at 150 K[10] in space group $P4_2/n$. When the structure is solved in this space group, there is one quarter of a tetraphenylmethane unit in the asymmetric unit, *i.e.* the tetraamidinium and tetracarboxylate tectons appear superimposed, and these groups needed to be modelled as disordered, as did the position of the hydrogen atoms on the water solvent molecules (in order to give sensible hydrogen bonding positions).

Using very intense synchrotron radiation at the MX2 beamline of the Australian Synchrotron,[12] we have now been able to obtain better intensity data, which suggest that the correct space group is actually the centred space group $I4_1/a$. Solving and refining in this centred space group gives one quarter of each of the tetraamidinium and tetracarboxylate tectons and three water molecules in the asymmetric unit, and does not require any modelling of disorder (Figure S8). The atom positions, bond lengths and hydrogen bonding parameters are almost identical in the $P4_2/n$ and $I4_1/a$ refinements, with the exception of the position of the amidinium nitrogen atoms and carboxylate oxygen atoms, which had to be restrained in the $P4_2/n$ refinement.

N–H and O–H hydrogen atoms were visible in the difference map and their positions were refined with restraints on bond lengths and angles; apart from the restraints on hydrogen atom positions, it was not necessary to use any crystallographic restraints in the refinement.

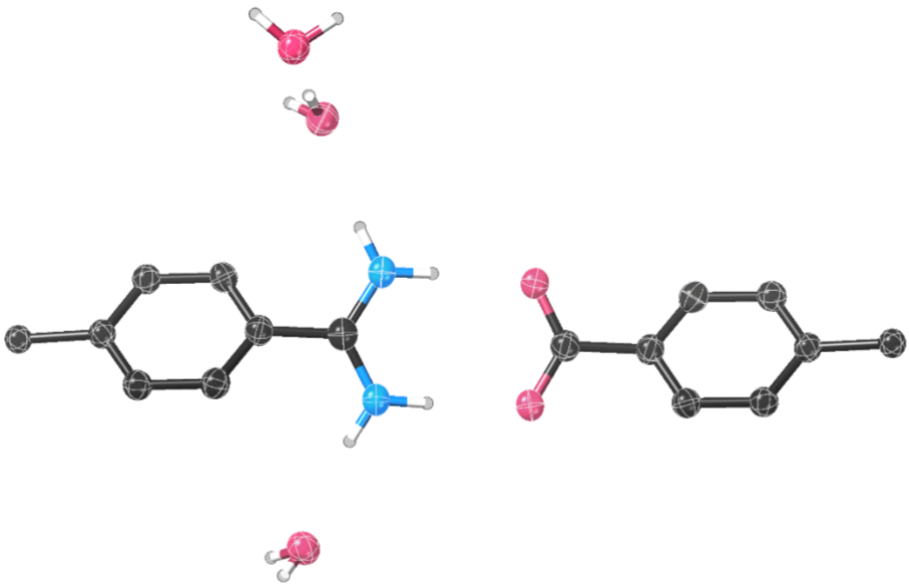

**Figure S8.** Thermal ellipsoid plot showing the asymmetric unit of **α-1$^{C/C}$** at 100 K; ellipsoids are shown at 50% probability, C–H hydrogen atoms are omitted for clarity.

**Structure of α-1$^{C/C}$ at 150 K:** This structure was collected using Cu radiation on a home-source X-ray diffractometer and refined in the $I4_1/a$ space group. N–H and O–H hydrogen atoms were visible in the difference map and their positions were refined with restraints on bond lengths and angles; apart from the restraints on hydrogen atom positions, it was not necessary to use any crystallographic restraints in the refinement.

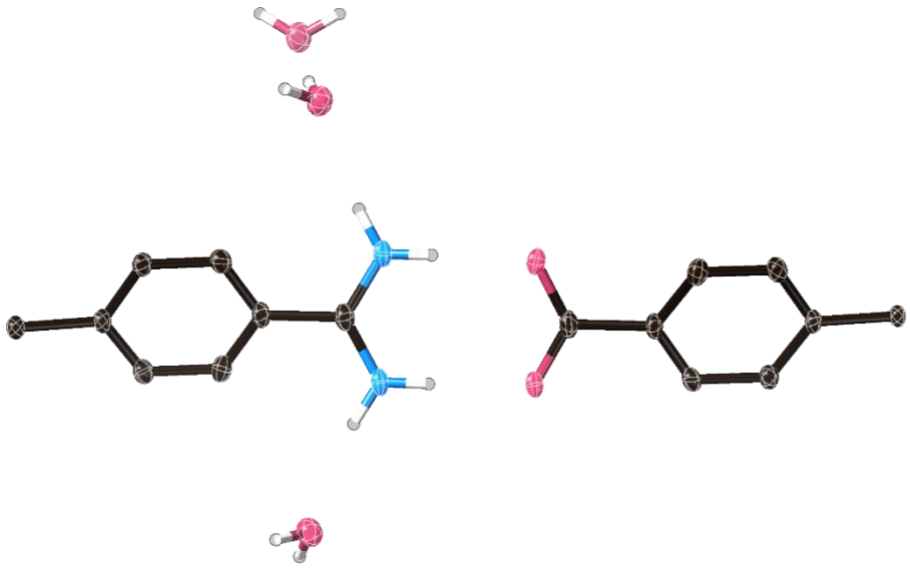

**Figure S9.** Thermal ellipsoid plot showing the asymmetric unit of **α-1$^{C/C}$** at 150 K; ellipsoids are shown at 50% probability, C–H t hydrogen atoms are omitted for clarity.

**Structure of α-1$^{C/C}$ at 273 K:** This structure was collected using the MX2 beamline of the Australian Synchrotron[12] and refined in the $I4_1/a$ space group. N–H and O–H hydrogen atoms were visible in the difference map and their positions were refined with restraints on bond lengths and angles; apart from the restraints on hydrogen atom positions, it was not necessary to use any crystallographic restraints in the refinement.

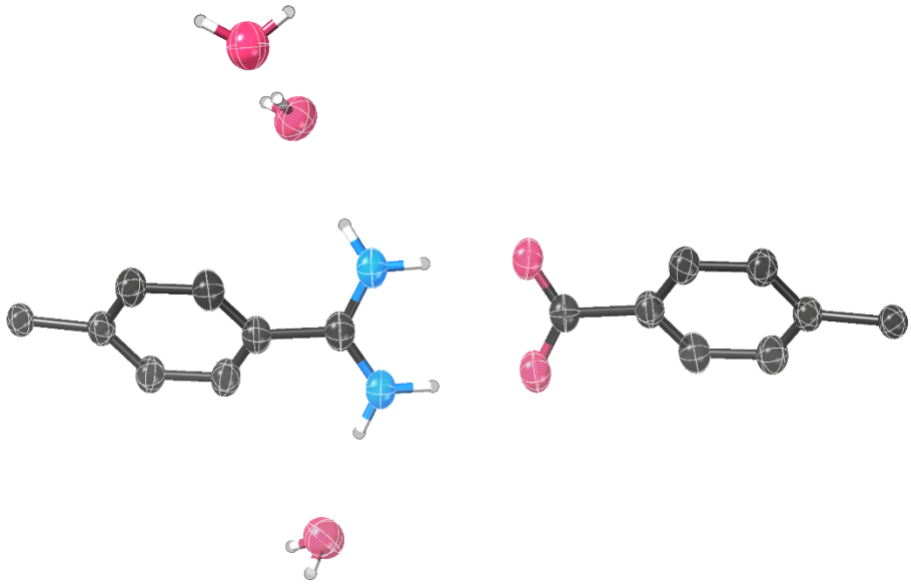

**Figure S10.** Thermal ellipsoid plot showing the asymmetric unit of **α-1$^{C/C}$** at 273 K; ellipsoids are shown at 50% probability, C–H hydrogen atoms are omitted for clarity.

**Structure of α-1$^{C/C}$ at 313 K:** This structure was collected using the MX1 beamline of the Australian Synchrotron[13] and refined in the $I4_1/a$ space group. Diffraction data could only be obtained to a resolution of 0.9 Å. N–H and all but one O–H hydrogen atoms were visible in the difference map and their positions were refined with restraints on bond lengths and angles; the remaining O–H hydrogen atom was inserted at an idealised hydrogen bonding position and then its position refined with restraints on bond lengths and angles. Apart from the restraints on hydrogen atom positions, it was not necessary to use any crystallographic restraints in the refinement.

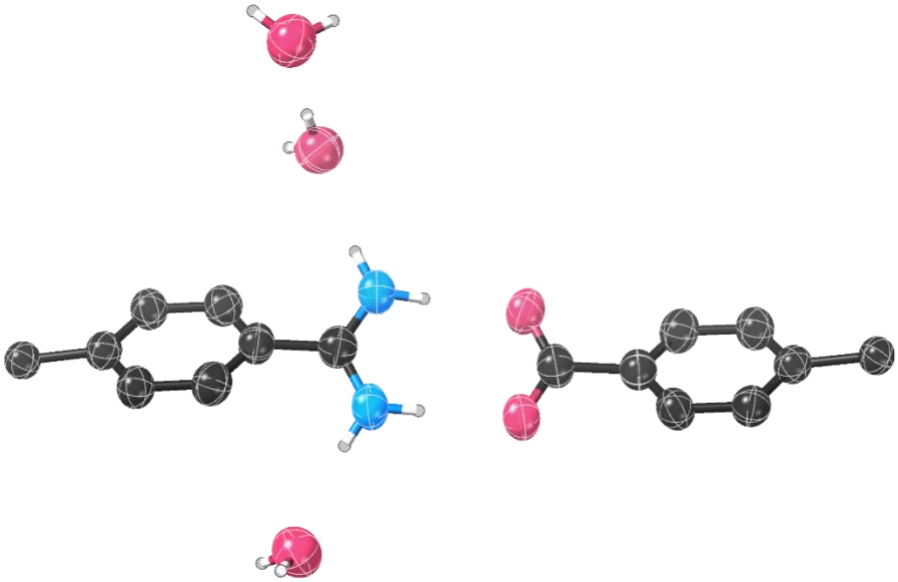

**Figure S11.** Thermal ellipsoid plot showing the asymmetric unit of **α-1$^{C/C}$** at 313 K; ellipsoids are shown at 50% probability, C–H hydrogen atoms are omitted for clarity.

**Structural comparison of α-1$^{C/C}$ at 100 K and 313 K:** The structures of **α-1$^{C/C}$** at 100 K and 313 K are compared in Figure S12. The structures are almost identical, and the positions of the water molecules are similar and well-ordered.

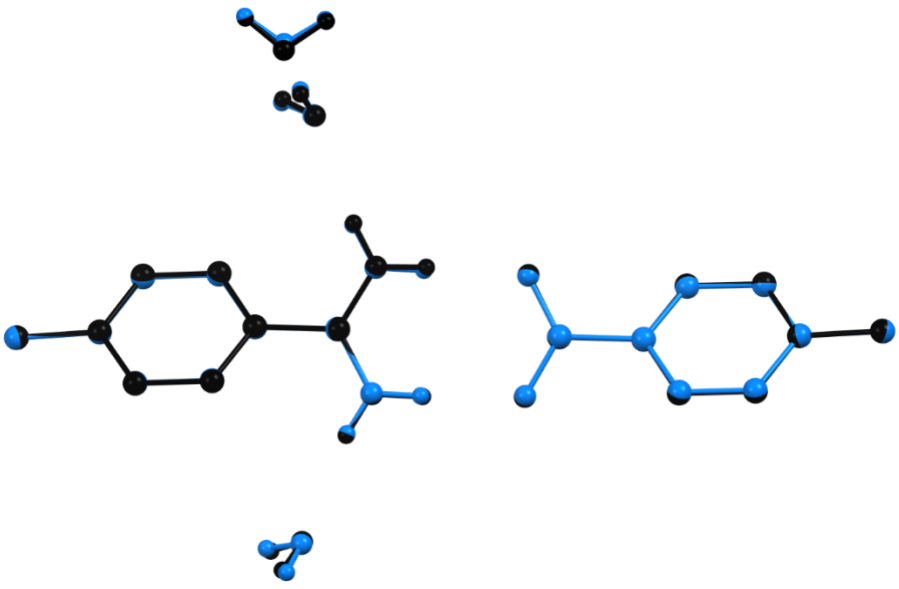

**Figure S12.** Overlay of the structures of **α-1$^{C/C}$** at 100 K (black) and 313 K (blue). C–H hydrogen atoms are omitted for clarity.

## *Structure of β-1$^{C/C}$*

Crystals of **β-1$^{C/C}$** were prepared by heating on a hotplate as described above. The structure was collected using the MX2 beamline of the Australian Synchrotron[12] at 100 K and solved and refined in the $P4_3$ space group. Crystals were relatively weakly diffracting and it was not possible to obtain diffraction data beyond 0.90 Å even using microfocus synchrotron radiation, The asymmetric unit cell contains one tetraphenylmethane-based molecule. As the tetraamidinium and tetracarboxylate tectons have very similar geometries, they are in the same place crystallographically (*i.e*. all carbon atoms overlap, and the O/N atoms of the carboxylate/amidinium groups essentially overlap). The structure was modelled by having eight half-occupancy oxygen atoms and eight half-occupancy nitrogen atoms (with attached hydrogen atoms). Due to the low quality of the data, it was necessary to impose restraints to all bond lengths, and all thermal and vibrational ellipsoid parameters. It was also necessary to restrain the bond angles of the amidinium and carboxylate groups.

There are two full occupancy water molecules and four half-occupancy water molecules: each of these half occupancy water molecules is located approximately 1.6 Å from another, *i.e*. there are two "pairs" of half-occupancy water molecules, presumably arising from different hydrogen bonding patterns. Due to the low quality of the data, C–H hydrogen atoms were inserted at calculated positions, and N–H and O–H hydrogen atoms were inserted at idealised hydrogen bonding positions. There are two hydrogen atom positions visible for the full occupancy water molecules, and so four hydrogen atoms were inserted for each of these waters with occupancies of 0.5 each. In the case of the hydrogen atoms on the half-occupancy water molecules, the hydrogen atom positions were not as clear and so these positions should be taken with caution. All hydrogen atoms ride on the attached non-H atoms.

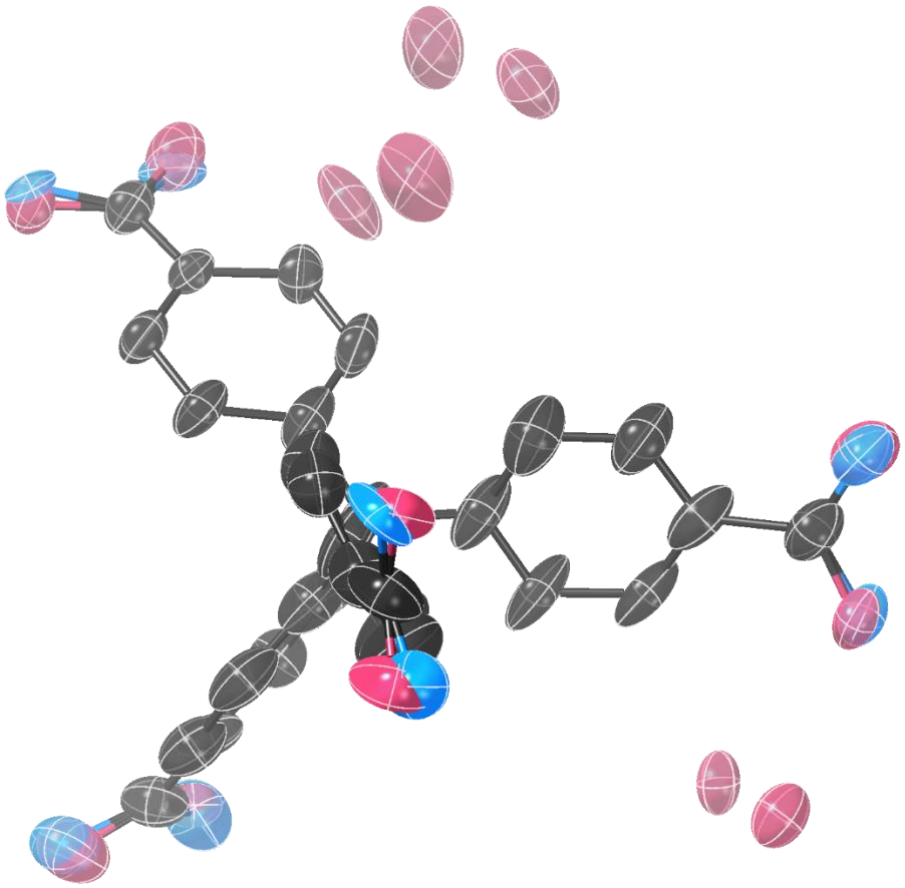

**Figure S13.** Thermal ellipsoid plot showing the asymmetric unit of **β-1$^{C/C}$**; ellipsoids are shown at 50% probability, hydrogen atoms are omitted for clarity.

## *Structure of γ-1$^{C/C}$*

The crystal structure of **γ-1$^{C/C}$** was obtained by holding crystals of **β-1$^{C/C}$** (prepared as described above) in the nitrogen stream of a home-source X-ray diffractometer at 318 K for an extended period (as described above). Diffraction was very weak and despite long exposure times and the use of Cu radiation, no data were observed beyond 1.1 Å. Nevertheless, the structure solved readily and a sensible and stable refinement could be achieved without the use of any restraints although bond lengths and angles were slightly irregular, *e.g.* phenyl C–C bond lengths ranged from 1.32 to 1.44 Å, and some ellipsoids were elongated. By adding restraints to bond lengths, bond angles, and thermal and vibrational ellipsoid parameters, a stable refinement with sensible bond lengths and angles could be achieved. Due to the low quality of the data, hydrogen atoms were inserted at calculated positions and ride on the attached atom.

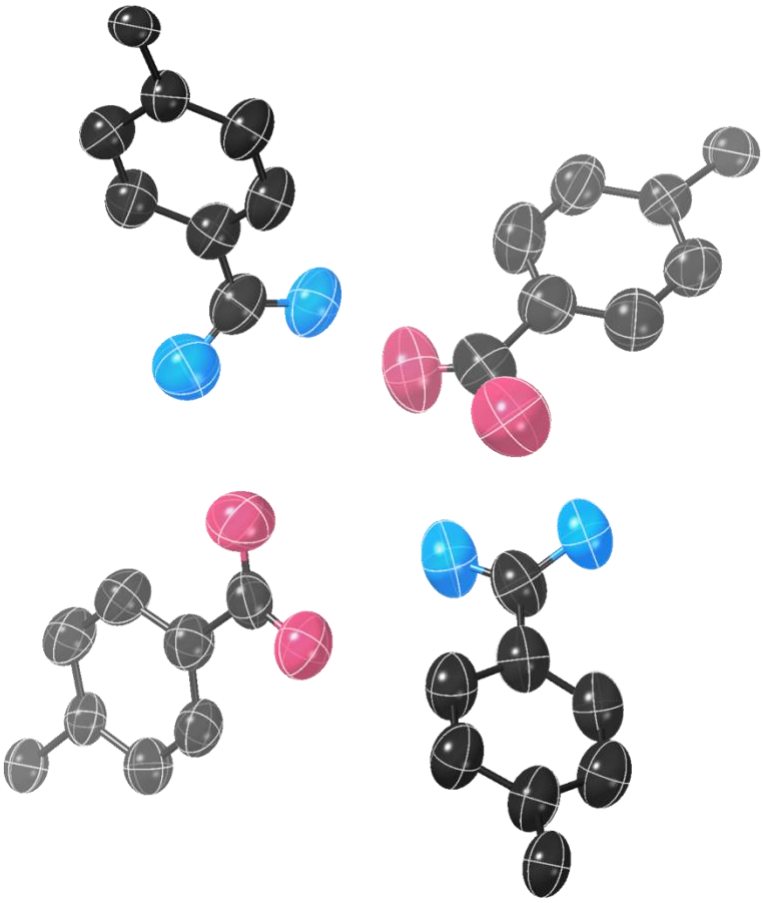

**Figure S14.** Thermal ellipsoid plot showing the asymmetric unit of **γ-1$^{C/C}$**; ellipsoids are shown at 50% probability, hydrogen atoms are omitted for clarity.

## *SCXRD structures and PXRD of 1$^{Si/C}$*

**SCXRD structure of α-1$^{Si/C}$:** We have previously reported this structure.[4] Data are available from the Cambridge Structural Database (CCDC: 2021300).

**SCXRD structure of triclinic-1$^{Si/C}$:** Crystals of **triclinic-1$^{Si/C}$** were solved and refined in the triclinic space group *P*–1; the asymmetric unit contains one entire tetraamidinium molecule and one entire tetracarboxylate molecule. It was possible to construct a crude model of the solvent present, which appears to be approximately 16 water molecules and three ethanol molecules (Figure S15). While this model could be constructed, it could not be refined satisfactorily, due to apparent positional disorder and partial occupancy of several of the solvent molecules. It should be noted that leaving these crystals out of the crystallisation liquor at room temperature causes their conversion to a tetragonal phase containing 12 well-ordered water molecules, so it is probably not surprising that the solvent molecules in this triclinic phase are not well-defined. As the solvent content could not be modelled satisfactorily, PLATON SQUEEZE[20] was used to include the solvent's electron density in the model. Once this was done, refinement proceeded smoothly (thermal ellipsoid plot shown in Figure S16) and apart from restraints on hydrogen atom positions (which were visible in the difference map and refined with restraints), it was not necessary to use any crystallographic restraints in the refinement.

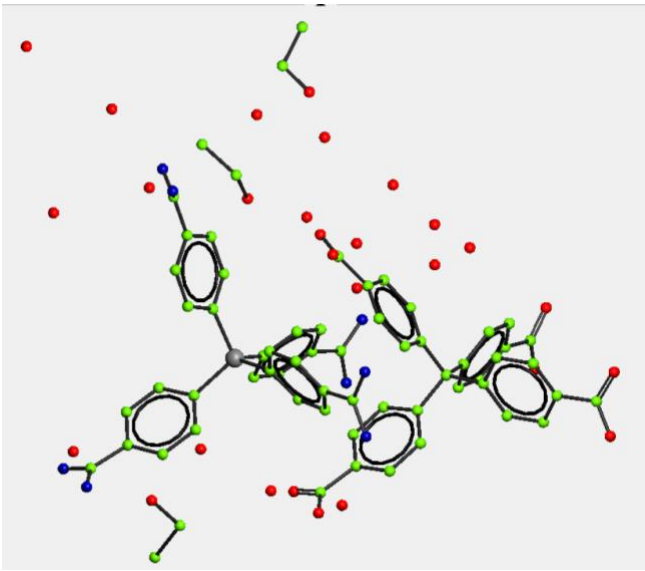

**Figure S15.** Partial refinement of the structure of **triclinic-1$^{Si/C}$** within Crystals[18] showing likely solvent positions.

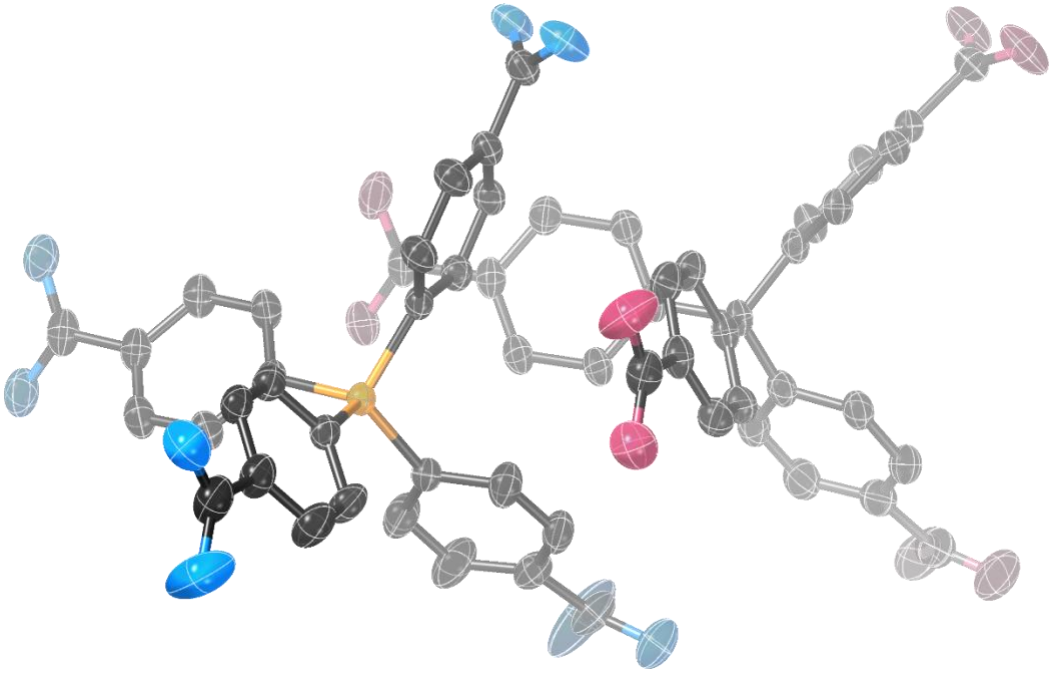

**Figure S16.** Thermal ellipsoid plot showing the asymmetric unit of **triclinic-1$^{Si/C}$**; ellipsoids are shown at 50% probability, hydrogen atoms are omitted for clarity. Note PLATON-SQUEEZE was used.[20]

**PXRD of triclinic-1$^{Si/C}$:** It was difficult to obtain PXRD data for the triclinic phase, due to its rapid conversion to the tetragonal **α-1$^{Si/C}$** phase upon removal from solvent. We took crystals from the crystallisation liquor, immediately covered them with oil and ran a PXRD trace; we then separately ran a PXRD trace of blank oil and subtracted this from the data. As can be seen in Figure S17, while this does not give high quality data, peaks that appear to match those calculated for **triclinic-1$^{Si/C}$** appear to be present, as well as peaks corresponding to **α-1$^{Si/C}$**.

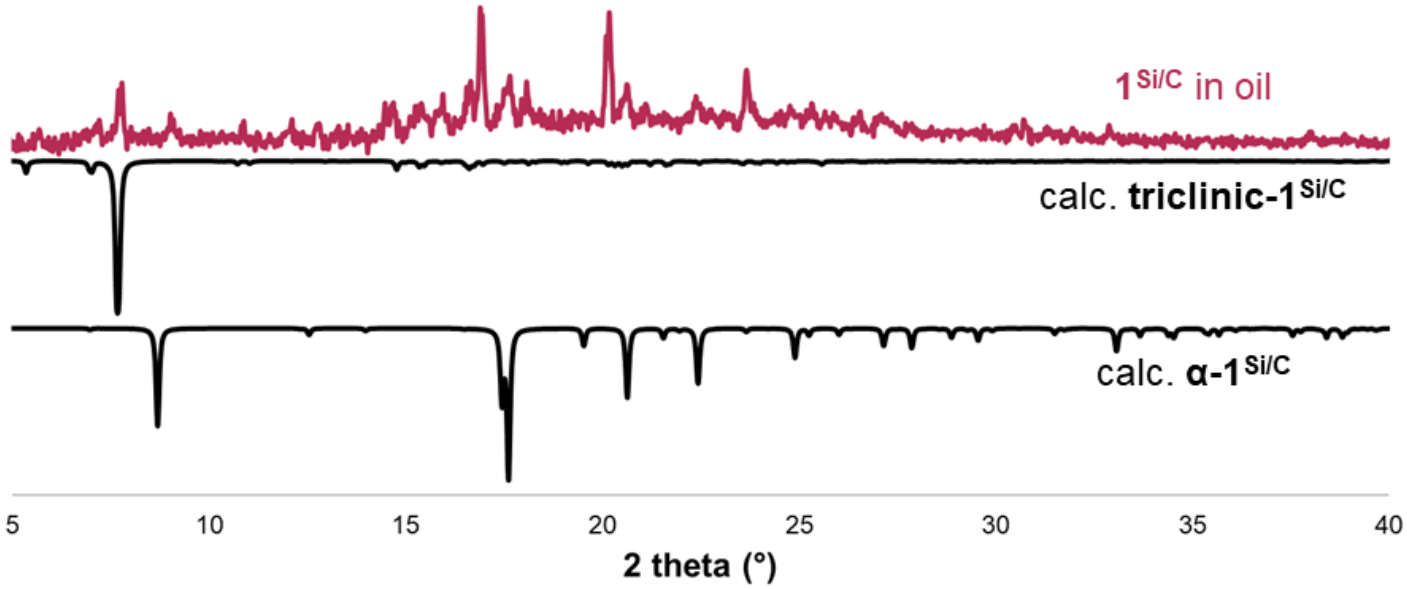


**Figure S17.** PXRD pattern of crystals of **1$^{Si/C}$** that were removed from the crystallization solvent and immediately covered in oil. A PXRD trace of the oil was also run and has been subtracted from the observed data.

## *SCXRD structures and PXRD of 1$^{Si/Si}$*

**SCXRD structure of α-1$^{Si/Si}$:** We have previously reported this structure.[5] Data are available from the Cambridge Structural Database (CCDC: 2151777).

**SCXRD structure of triclinic-1$^{Si/Si}$:** Crystals of **triclinic-1$^{Si/Si}$** were solved and refined in the triclinic space group *P*–1 and the asymmetric unit contains one entire tetraamidinium molecule and one entire tetracarboxylate molecule. It was possible to construct a crude model of the solvent present, which appears to be approximately 16 water molecules and three ethanol molecules (Figure S18). While this model could be constructed, it could not be refined satisfactorily, due to apparent positional disorder and partial occupancy of several of the solvent molecules. It should be noted that leaving these crystals out of the crystallisation liquor at room temperature causes their conversion to a tetragonal phase containing 12 well-ordered water molecules, so it is probably not surprising that the solvent molecules in this triclinic phase are not well-defined. As the solvent content could not be modelled satisfactorily, PLATON SQUEEZE[20] was used to account for the solvent's electron density in the model. Once this was done, refinement proceeded smoothly (thermal ellipsoid plot shown in Figure S19) and apart from restraints on hydrogen atom positions (which were visible in the difference map and refined with restraints), it was not necessary to use any further restraints in the refinement.

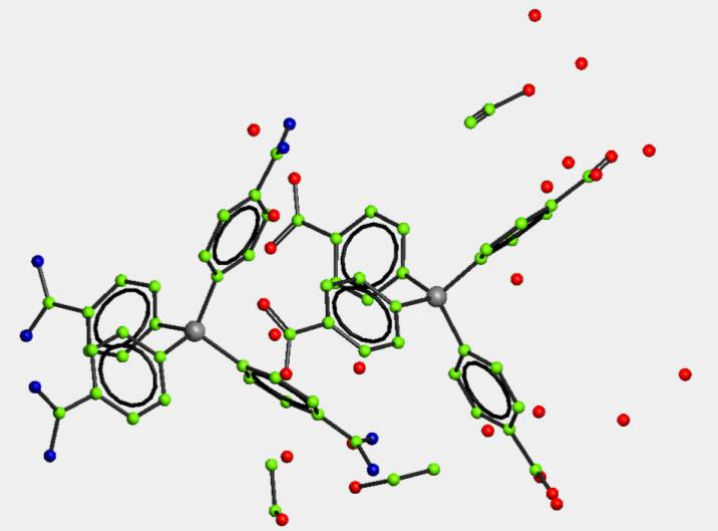

**Figure S18.** Partial refinement of the structure of **triclinic-1$^{Si/Si}$** within Crystals[18] showing proposed solvent positions.

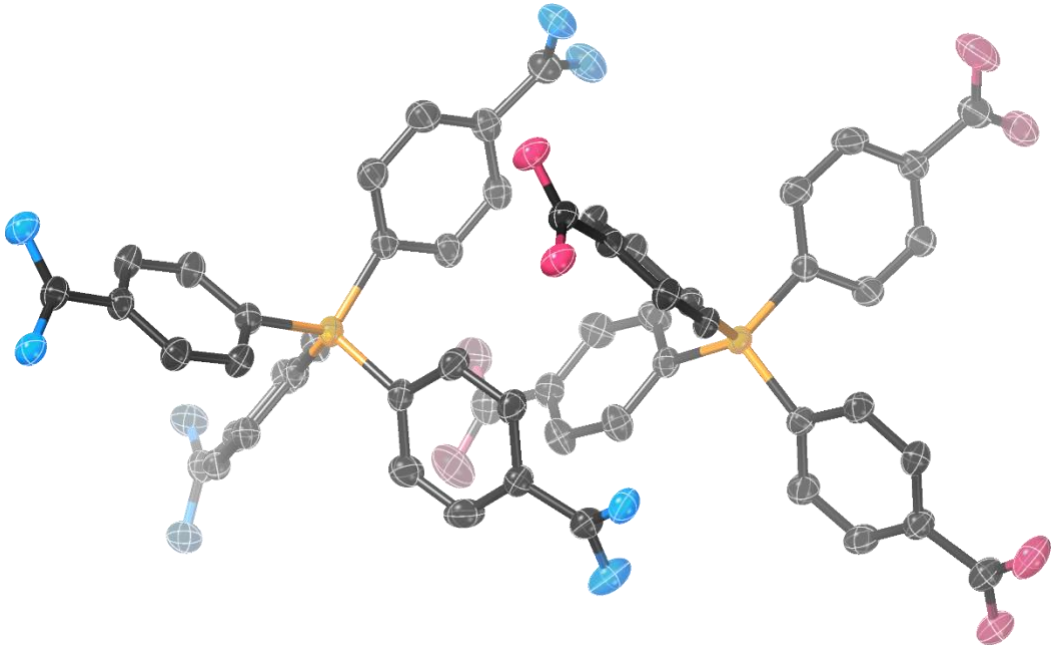

**Figure S19.** Thermal ellipsoid plot showing the asymmetric unit of **triclinic-1$^{Si/Si}$**; ellipsoids are shown at 50% probability, hydrogen atoms are omitted for clarity. Note PLATON-SQUEEZE was used.[20]

**PXRD of triclinic-1$^{Si/Si}$:** It was difficult to obtain PXRD data for the triclinic phase, due to its rapid conversion to the tetragonal phase upon removal from solvent. We took crystals from the crystallisation liquor, immediately covered them with oil and ran a PXRD trace; we then separately ran a PXRD trace of blank oil and subtracted this from the data. As can be seen in Figure S20, while this material is crystalline, it is not obvious which phase of the material is present at this point, and indeed it may be an as-yet-unidentified phase of **1$^{Si/Si}$**.

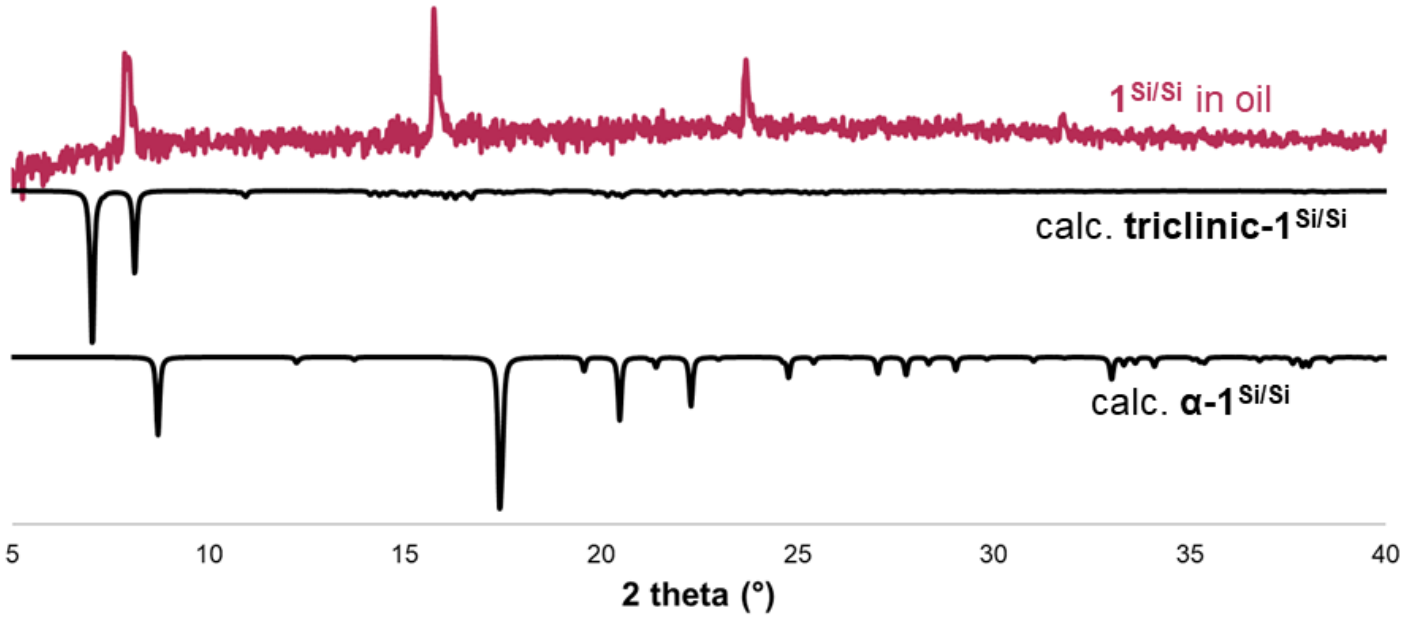


**Figure S20.** PXRD pattern of crystals of **1$^{Si/Si}$** that were removed from the crystallization solvent and immediately covered in oil. A PXRD trace of the oil was also run and has been subtracted from the observed data.

# Thermogravimetric analysis and water sorption

The full TGA-DSC plot for **1**$^{C/C}$ is shown in Figure S21 (a truncated version is provided in the main manuscript).

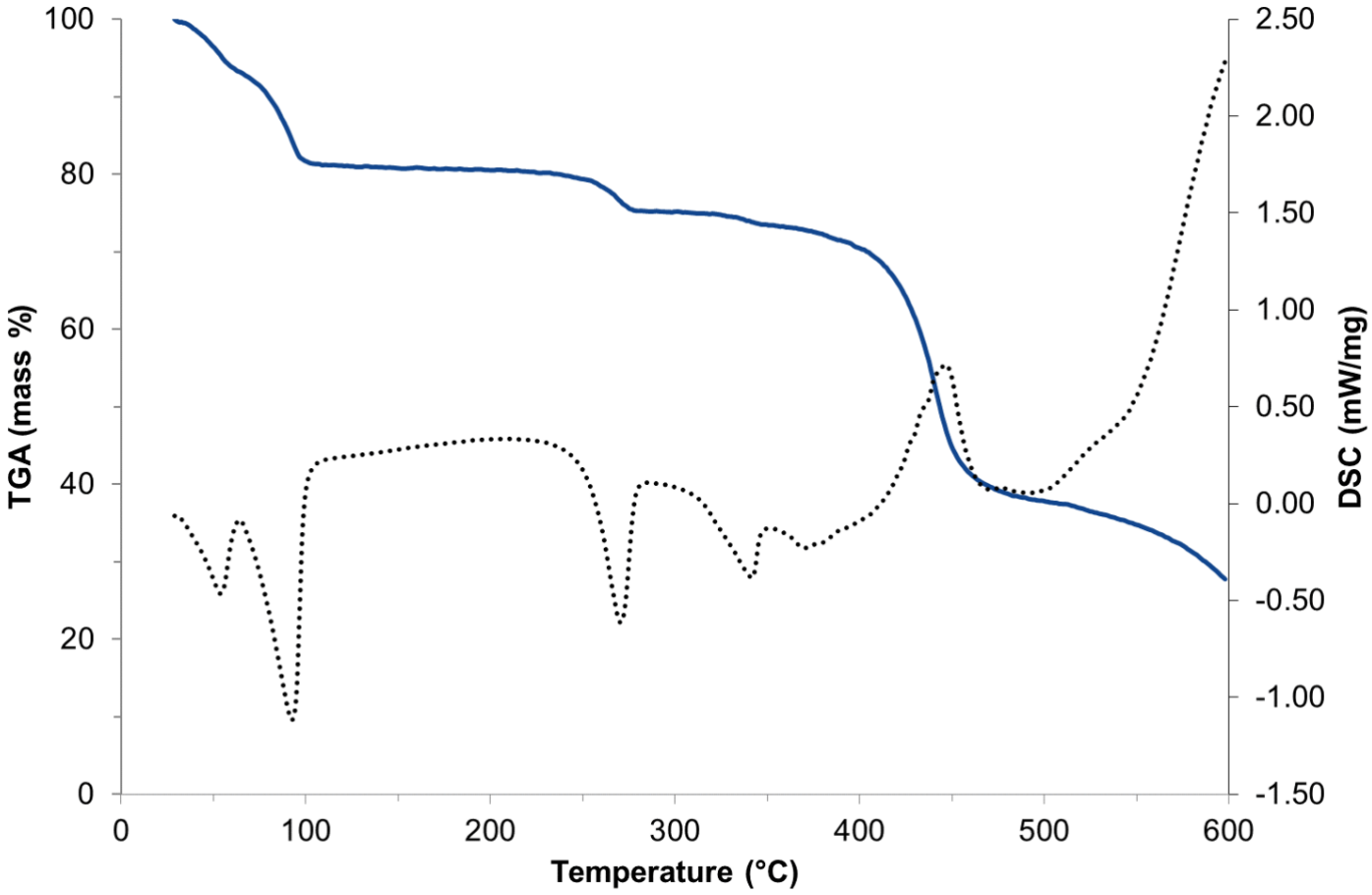


**Figure S21.** TGA-DSC plot of **1**$^{C/C}$ showing mass losses (blue line) and associated energy changes (dotted black line).

A comparison of the TGA traces for as-synthesized (*i.e.* α) **1**$^{C/C}$, **1**$^{Si/C}$ and **1**$^{Si/Si}$ are provided in Figure S22. As can be seen, the mass losses occur at the lowest temperature for **1**$^{Si/Si}$ and the highest temperatures for **1**$^{C/C}$. Clear mass loss "steps" corresponding to the α to β transition and subsequent β to γ transition are observed, and under flowing nitrogen these mass losses begin close to room temperature.

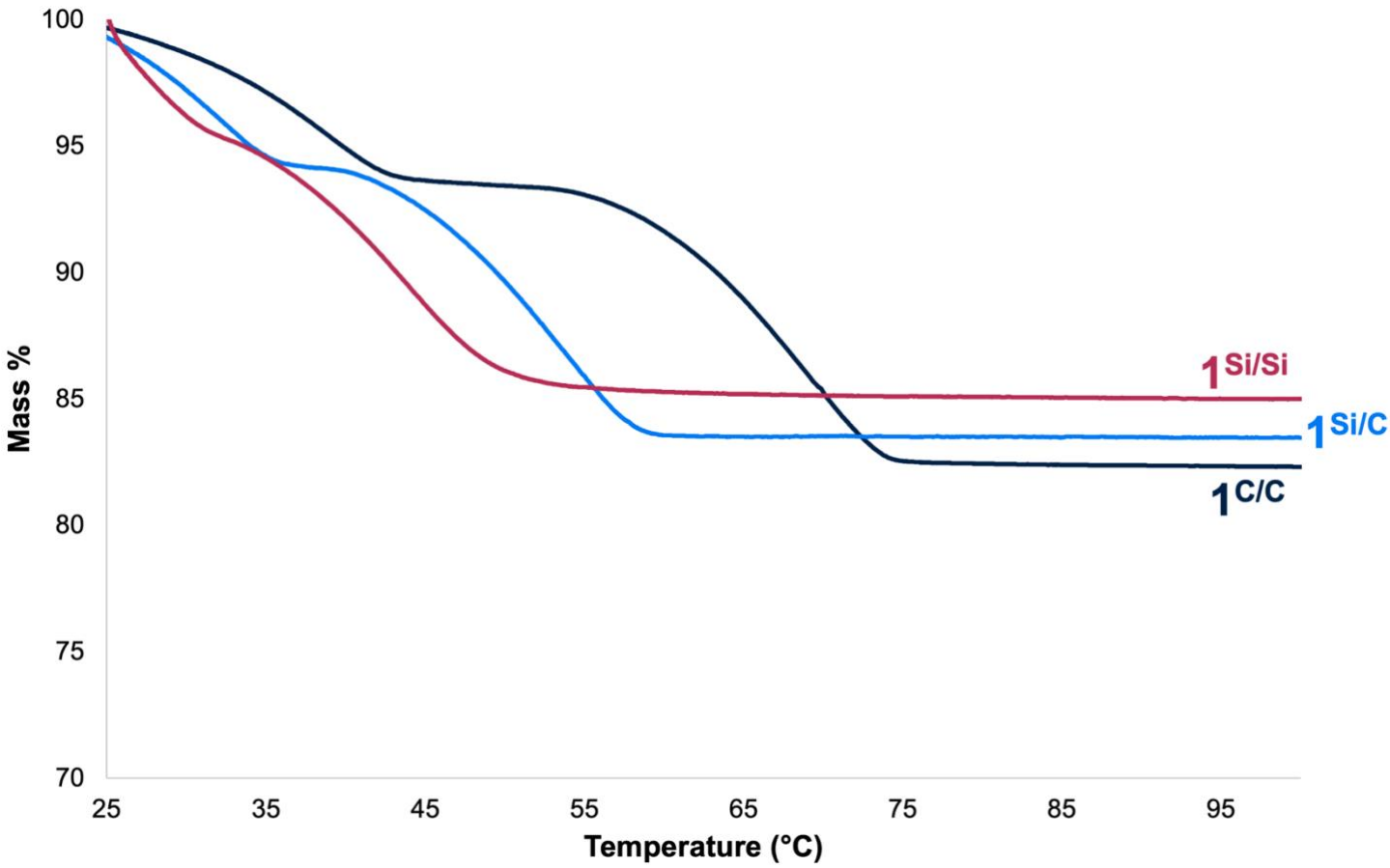


**Figure S22.** TGA traces of **α-1**$^{C/C}$, **α-1**$^{Si/C}$ and **α-1**$^{Si/Si}$. All traces recorded under $N_2$ at 5 °C/minute.

Figures S23–S25 compare the TGA traces of the as-synthesized α phases of each framework with the traces obtained after the VT-PXRD studies, *i.e.* the β-phases. The α-phases exhibit three well-defined mass losses in the 25–275 °C range: two stepwise water losses at temperatures below 100 °C to give the anhydrous frameworks, and then loss of four molecules of $NH_3$ per amidinium component to give the tetranitrile.[21] In contrast, the β-phases show two well-defined mass losses, one corresponding to water and the other to ammonia. We observed slight variabilities in the water content of the α-phases of the frameworks (typically ±1–2 water molecules), which we attribute to different ambient humidities. Both **β-1**$^{C/C}$ and **β-1**$^{Si/C}$ contain eight water molecules per formula unit, while **β-1**$^{Si/Si}$ contains only three water molecules, which we attribute to incomplete water uptake eight days after the VT-PXRD studies (when TGA data for this phase were recorded).

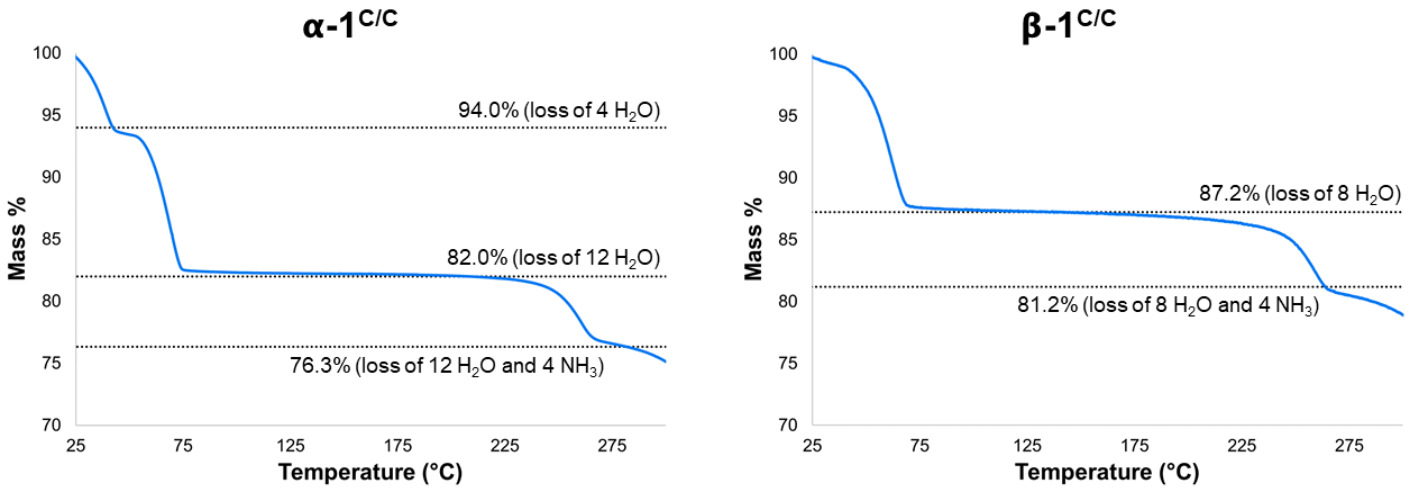


**Figure S23.** TGA traces of **α-1$^{C/C}$** and **β-1$^{C/C}$**. Expected mass losses corresponding to water solvent losses from framework and subsequent loss of $NH_3$ from amidinium motif are shown as dotted lines. Traces recorded under $N_2$ at 5 °C/minute.

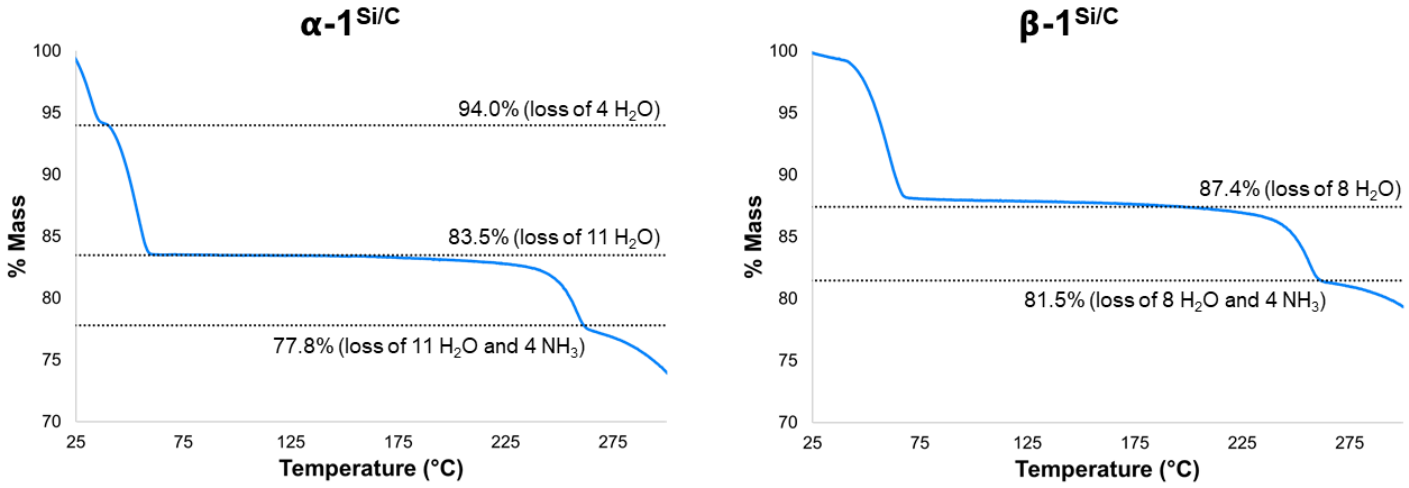


**Figure S24.** TGA traces of **α-1$^{Si/C}$** and **β-1$^{Si/C}$**. Expected mass losses corresponding to water solvent losses from framework and subsequent loss of $NH_3$ from amidinium motif are shown as dotted lines. Traces recorded under $N_2$ at 5 °C/minute.

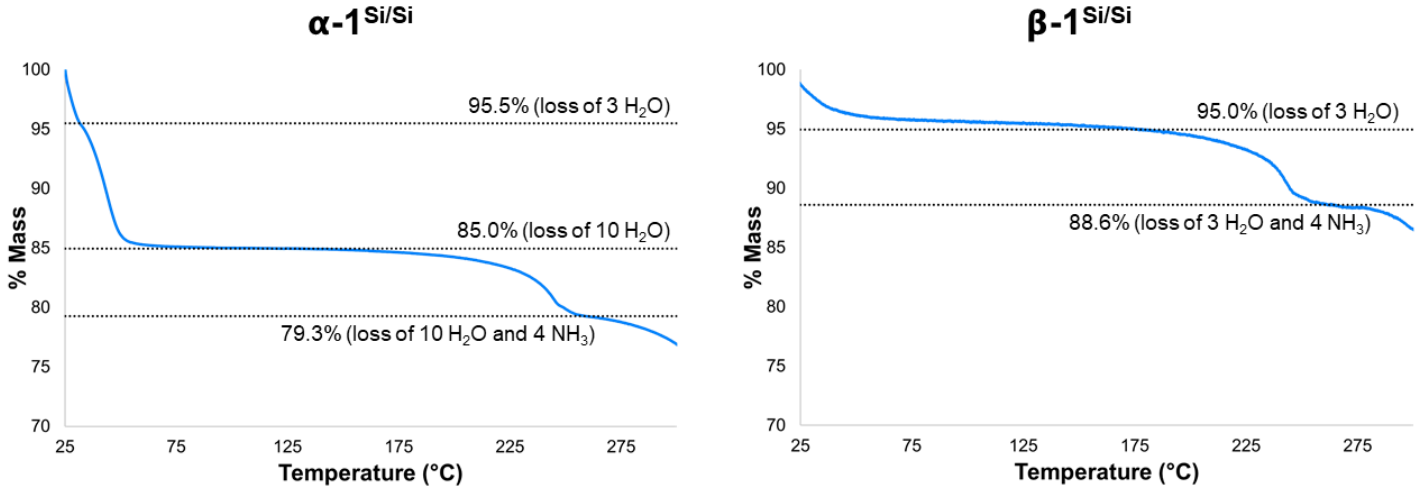


**Figure S25.** TGA traces of **α-1$^{Si/Si}$** and **β-1$^{Si/Si}$**. Expected mass losses corresponding to water solvent losses from framework and subsequent loss of $NH_3$ from amidinium motif are shown as dotted lines. Traces recorded under $N_2$ at 5 °C/minute.

The response of **γ-1**$^{C/C}$ to humidity was studied using TG-DSC at 40 °C under flowing conditions. The TG-DSC data are shown in Figure S26 and shown as an isotherm in the manuscript. The sample was heated to 130 °C in the TG-DSC instrument and then kept under flow of dry $N_2$ while the MHG was connected. The humidity protocol started at 5% RH and raised to 10% RH and then in 10% increments to 80% RH on the adsorption leg. The desorption leg was from 70% RH to 10% RH in 10% increments and then to 5% RH.

Up to 10% RH there is the adsorption of ~2% (~1 water molecule for **1**$^{C/C}$·$H_2O$) and at 20% RH this increases to 14.5% corresponding to **1**$^{C/C}$·$8H_2O$ i.e. **β-1**$^{C/C}$. There are no significant adsorption steps up to 80% RH at which point the compound can be formulated as **1**$^{C/C}$·$9H_2O$ from a further surface-bound water molecule. The desorption leg shows this is removed but the compound does not undergo β to γ restructuring down to 5% RH.

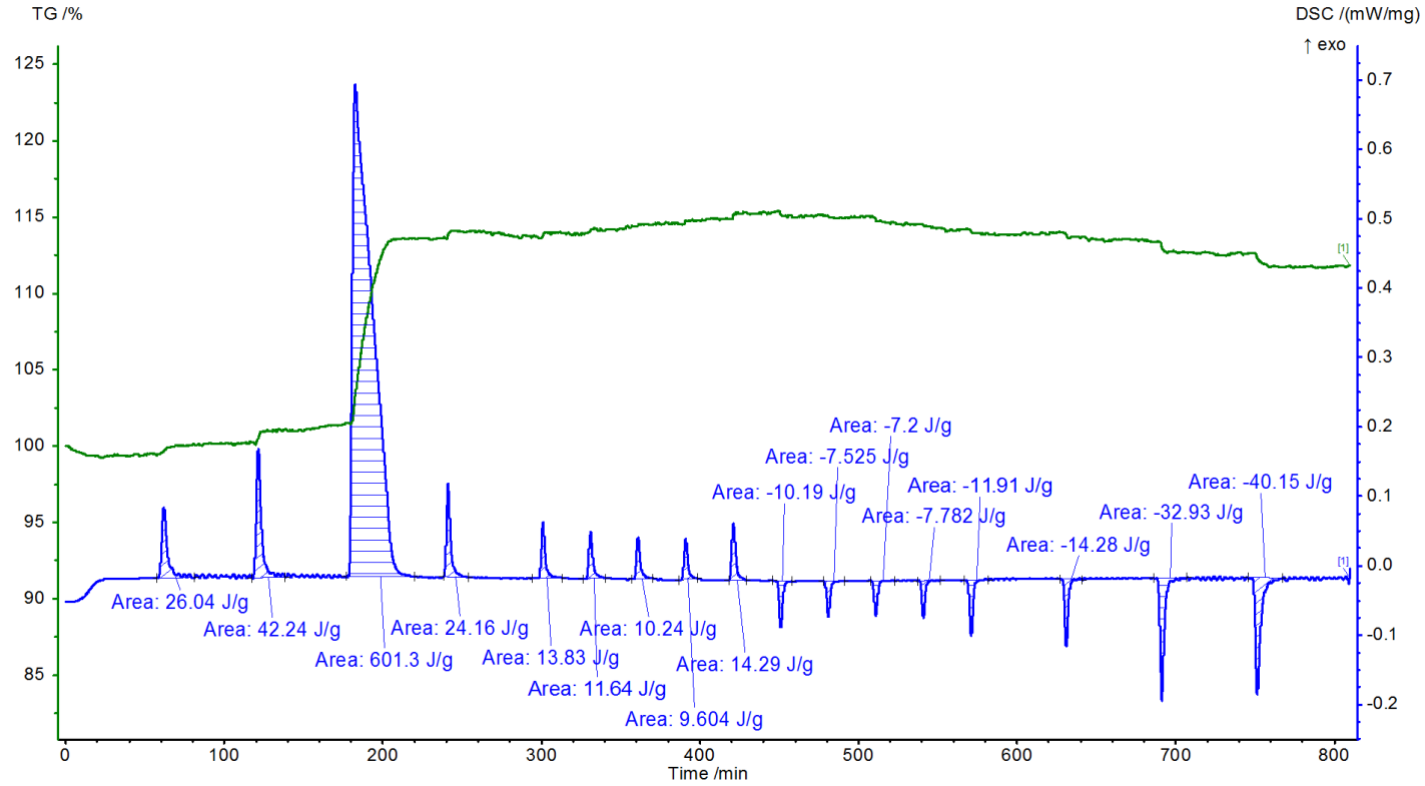


**Figure S26.** TG-DSC water vapour data for γ-**1**$^{C/C}$. The sample was heated to 130 °C in the TG-DSC instrument and then connected to the MHG under flow of dry $N_2$. The humidity protocol started at 5% RH and raised to 10% RH and then in 10% increments to 80% RH on the adsorption leg. The desorption leg was from 70% RH to 10% RH in 10% increments and then to 5% RH. TG data shown as the green line. The DSC data are shown in the blue trace with adsorption/desorption energies for the shaded areas.

The response of **α-1$^{C/C}$** to varying humidity was studied using TG-DSC at 40 °C under flowing conditions. The TG-DSC data are shown in Figure S27 and are plotted as an isotherm in Figure S28. The framework was held at 80% relative humidity (RH) for one hour, and then the humidity decreased in 10% increments. Between RH = 30% to 10%, a significant mass loss corresponding to six water molecules is observed, consistent with conversion to **β-1$^{C/C}$**, containing six waters (consistent with the six possible water sites observed in the SCXRD structure of this framework). Increasing the humidity to 30% does not reverse this showing that once formed, the β-phase does not revert to the α-phase. Increasing the relative humidity to 80% sees the framework take up two water molecules, *i.e.* returning to the eight water molecules observed by TGA. Taken together, the data are consistent with **β-1$^{C/C}$** containing six water molecules in its channels, and a further two surface-bound water molecules.

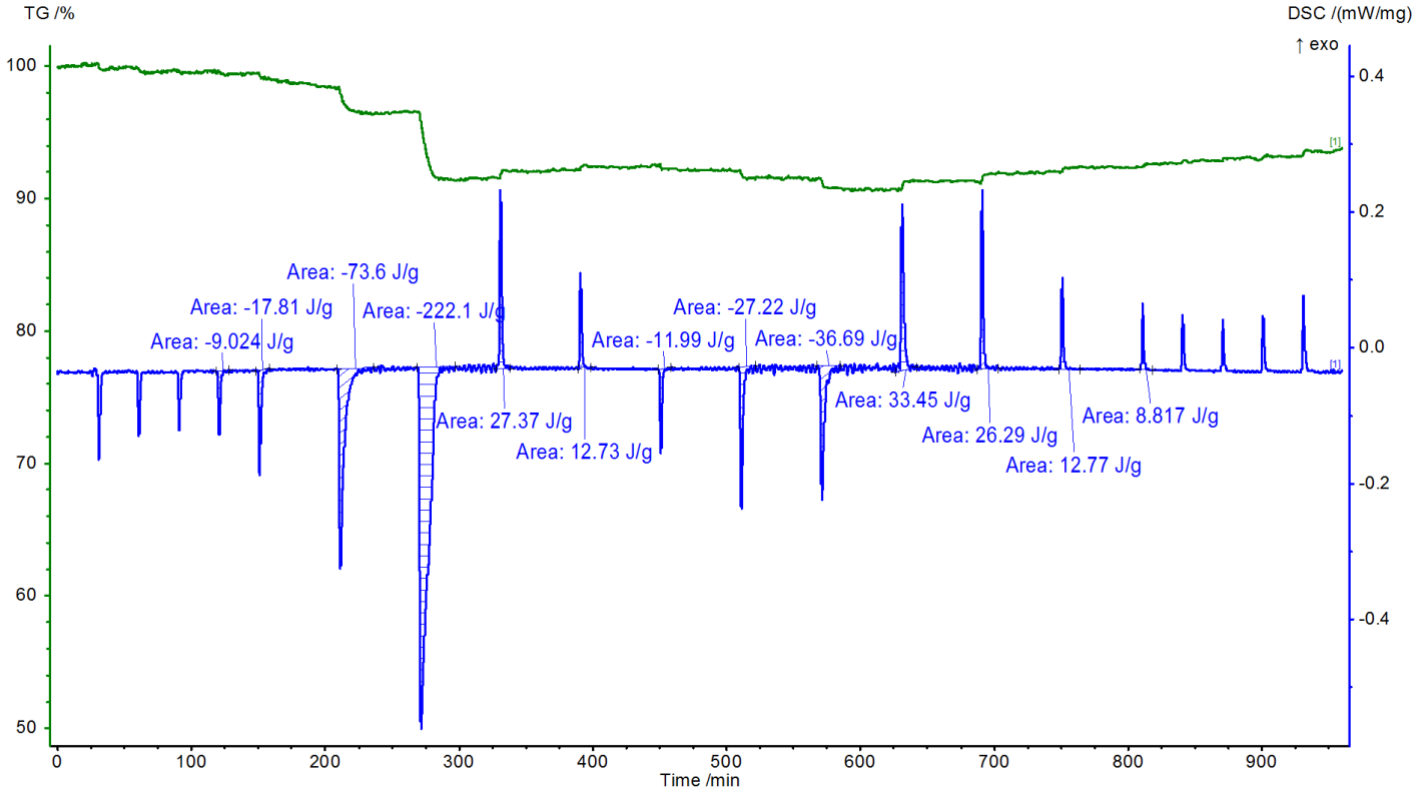


**Figure S27.** TG-DSC water vapour data for α-**1$^{C/C}$**. The RH is decreased in 10% increments from 80% RH to 10% RH then raised to 30% RH in 10% increments then decreased to 10% RH in 10% increments and further to 5% RH. The RH for the final adsorption is raised to 10%RH and to 80% RH in 10% increments. TG data shown as the green line. The DSC data are shown in the blue trace with adsorption/desorption enthalpies for the shaded areas.

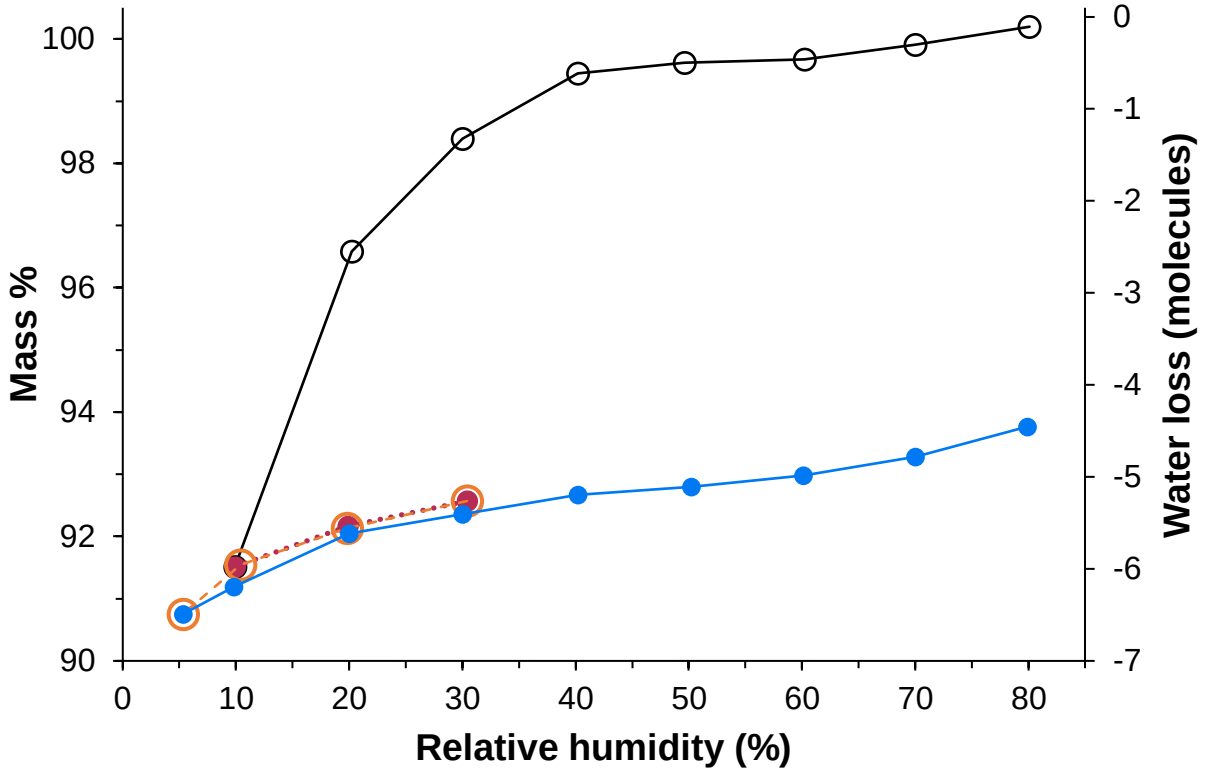


**Figure S28.** Isotherm of **α-1$^{C/C}$** in response to changes in humidity (filled circles represent adsorption, open circles represent desorption, coloured lines are provided to guide the eye). **α-1$^{C/C}$** is held at 80% RH for 1 hour and then the RH decreased in 10% increments to 10% RH (black open symbols). The RH is then raised to 30% RH in 10% increments (orange filled symbols). The RH is then decreased from 30% RH to 10% RH in 10% increments and further to 5% RH (red open symbols). The RH is then increased back to 80% RH for the final adsorption leg (blue filled symbols).

Water sorption of a bulk sample of **γ-1**$^{C/C}$ was studied gravimetrically in the atmosphere. A sample of **α-1**$^{C/C}$ (0.222 g) was placed in a 20 mL scintillation vial (diameter: 28 mm) and converted to the γ-phase by heating at 50 °C under a dynamic vacuum (~ 5 mbar) for one hour. This resulted in a mass loss of 16.7% consistent with the loss of 11 water molecules (expected: 16.8%). The sample was then placed on a balance in the same scintillation vial and its mass increase studied over time (approx. temperature: 23 °C, approx. RH: 48%, Figure S29). A mass gain of 14.4% was observed over approximately 300 minutes consistent with sorption of eight water molecules and conversion to the β-phase (expected: 14.6%). Heating this sample at 50 °C under a dynamic vacuum (~ 5 mbar) for one hour resulted in a mass loss of 14.4% consistent with removal of all water molecules. When this sample was exposed to the atmosphere again (approx. temperature: 23 °C, approx. RH: 50%), a similar mass gain (14.8%, expected for 8 $H_2O$: 14.6%) was observed at a broadly similar rate.

Accessibility to the atmosphere and the RH clearly affects the rate of water sorption: when a sample was tipped onto a watch glass, the sorption was largely complete within 10 minutes, while in multilayers on a PXRD sample holder, the phase change is largely complete within 30 minutes (Figure S29).

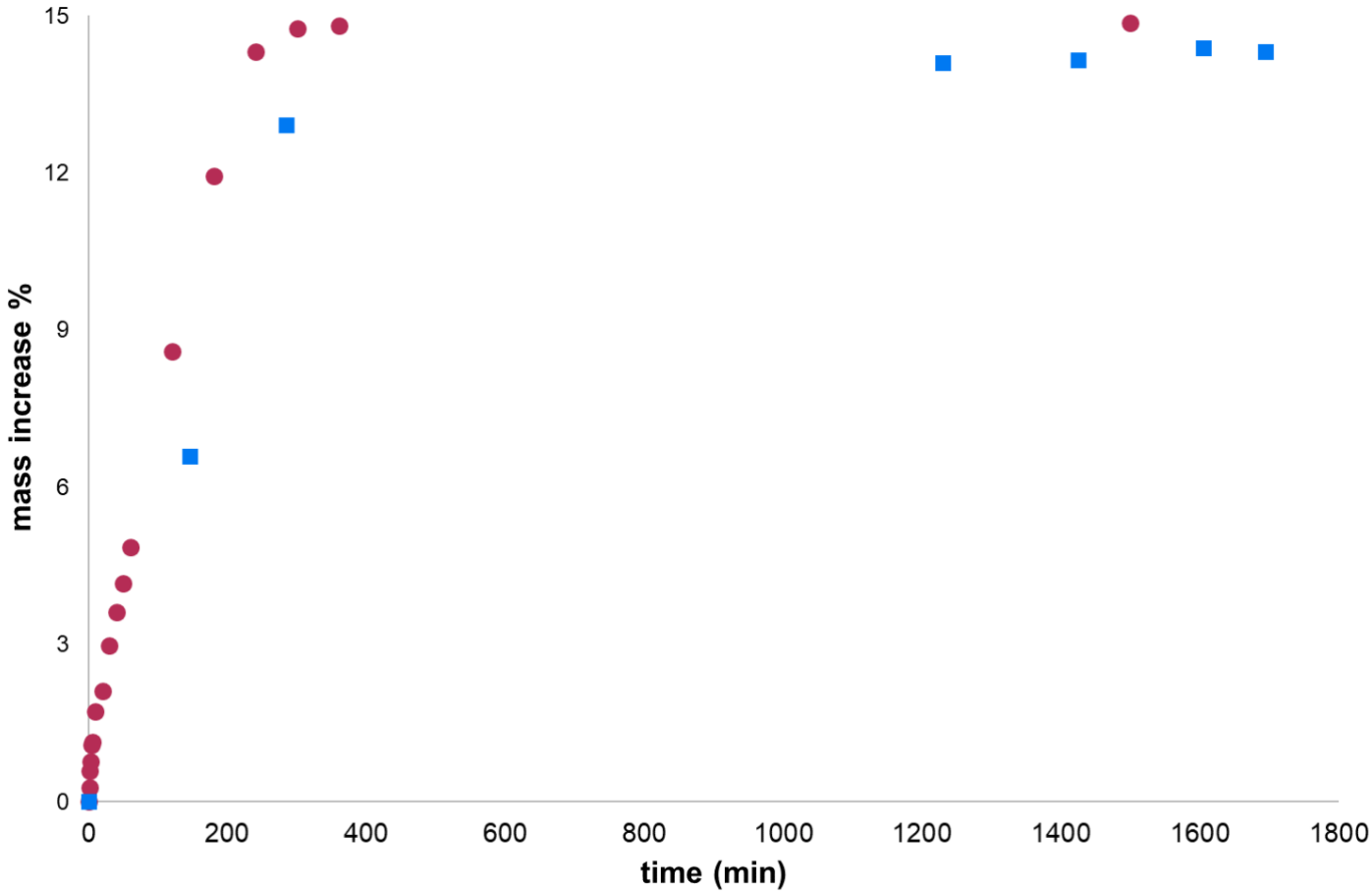


**Figure S29.** Mass increases of a sample of **γ-1**$^{C/C}$ on exposure to the atmosphere. The same sample was used for both runs: first run, RH ~ 48% shown as blue squares; second run, RH ~ 50% shown as red circles.

# Variable temperature PXRD

PXRD data were collected over the temperature range 30 – 130 °C in 10 °C increments. The sample was warmed to the given temperature, held at this temperature for five minutes, and then PXRD patterns recorded over approximately five minutes. Following this protocol, samples were raised from 30 to 130 °C and then cooled back down to 30 °C and held at this temperature. Figures S30–S32 show for all three frameworks the α to β transition occurs by 50 °C while the transition from β to γ is complete by 90 °C for **1**$^{C/C}$, 80 °C for **1**$^{Si/C}$ and 70 °C for **1**$^{Si/Si}$. The speed of the conversion from γ to β is essentially complete within 90 minutes for **1**$^{C/C}$, while for **1**$^{Si/C}$ this process is incomplete after 90 minutes but complete after 24 hours. For **1**$^{Si/Si}$, the γ to β transition is not apparent after 20 hours at 30 °C; after this point, the sample was held at room temperature, and the conversion back to the γ form is not entirely complete after 7 days, although does eventually go to completion after extended periods.

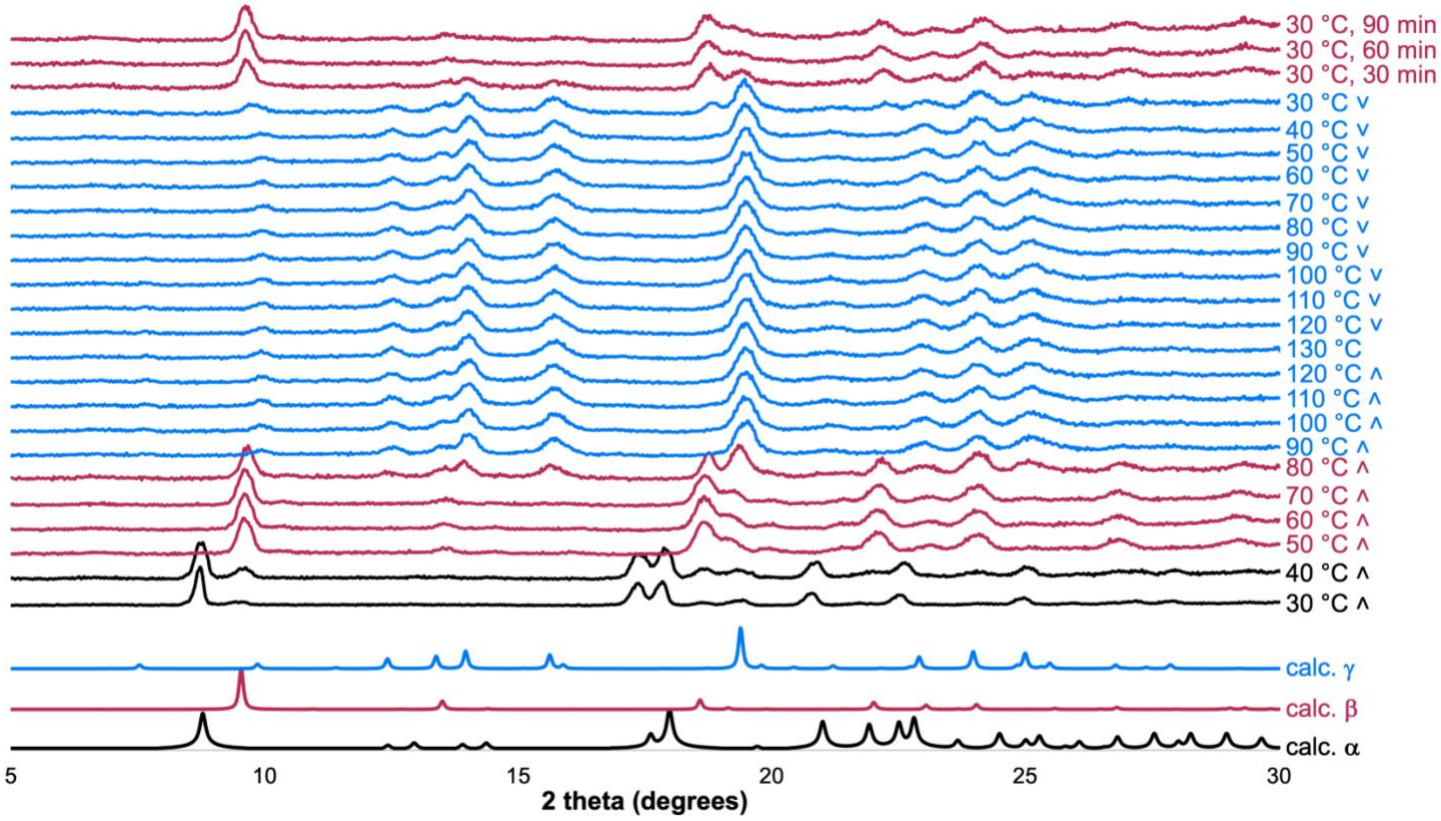


**Figure S30.** Variable temperature PXRD patterns of **1**$^{C/C}$ Patterns calculated based on the SCXRD structures of **α-1**$^{C/C}$, **β-1**$^{C/C}$ and **γ-1**$^{C/C}$ are provided for reference. The predominant phase is indicated by the colour of the trace (black = α, red = β, blue = γ).

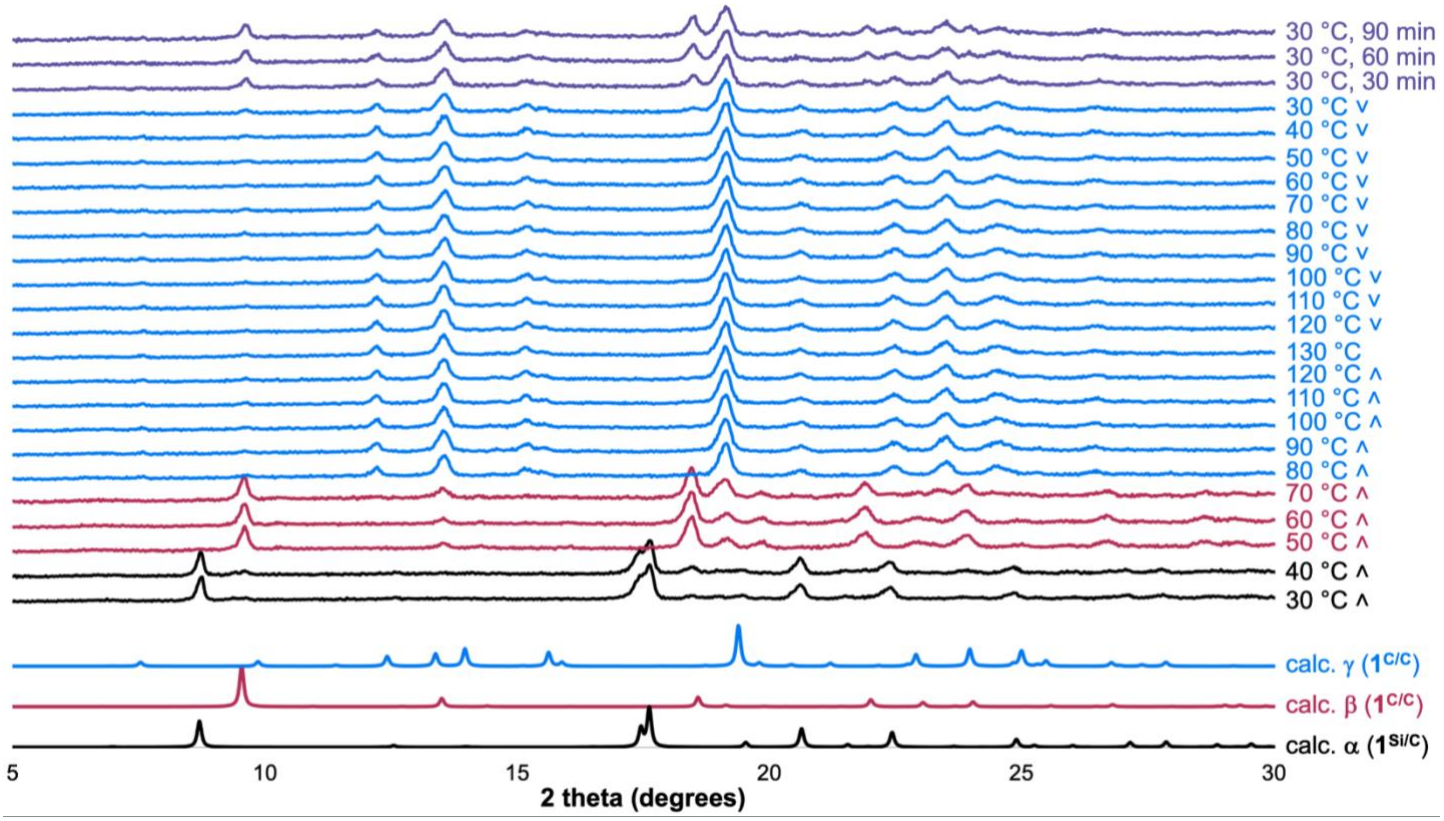


**Figure S31.** Variable temperature PXRD of $\mathbf{1}^{Si/C}$. Patterns calculated based on the SCXRD structures of $\mathbf{\alpha\text{-}1}^{Si/C}$, $\mathbf{\beta\text{-}1}^{C/C}$ and $\mathbf{\gamma\text{-}1}^{C/C}$ are provided for reference. The predominant phase is indicated by the colour of the trace (black = α, red = β, blue = γ, purple = mixture of α and β). The sample returned to the β phase within 24 hours.

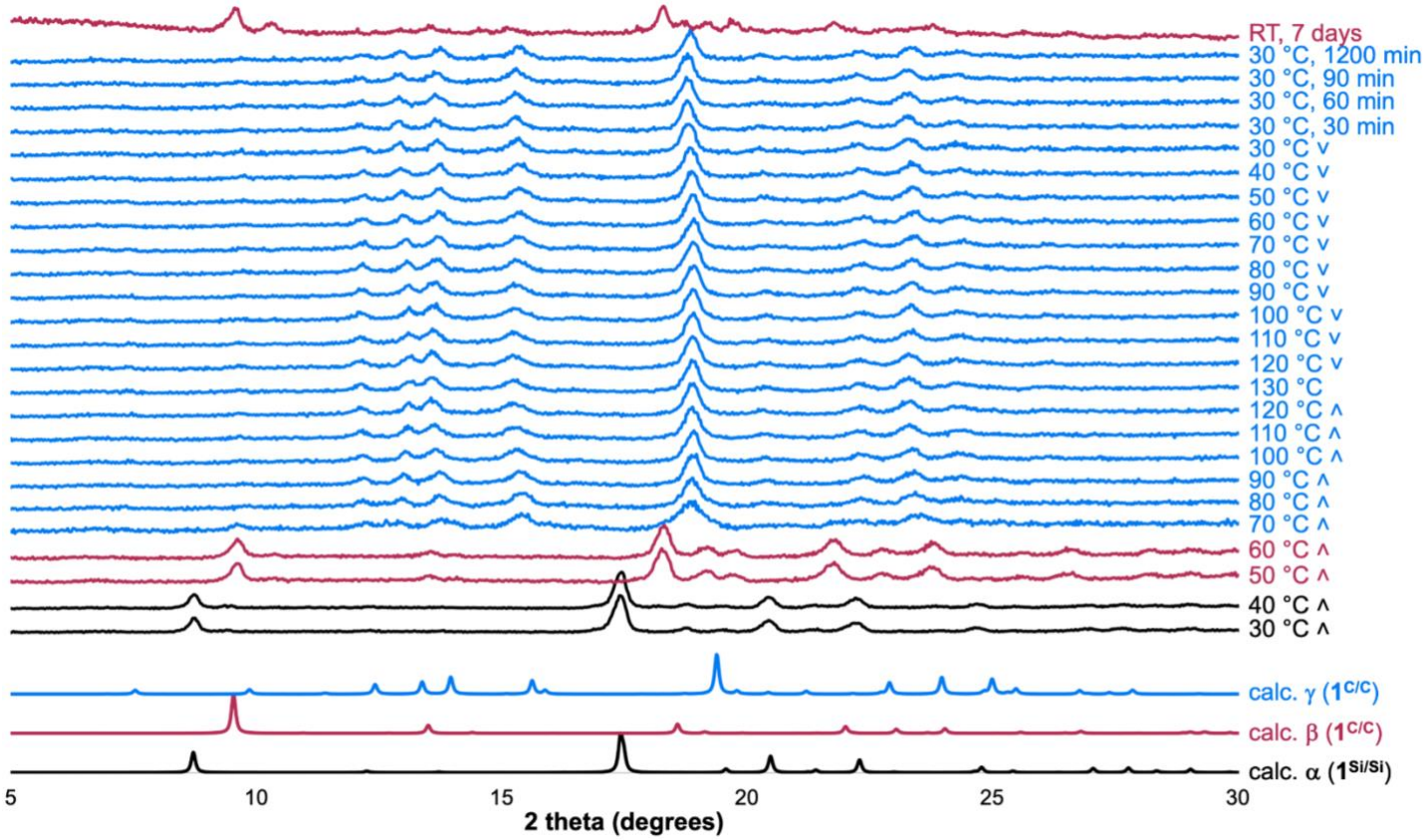


**Figure S32.** Variable temperature PXRD patterns of $\mathbf{1}^{Si/Si}$. the sample was heated from 30 °C to 130 °C then cooled back to 30 °C and held at this temperature for 1200 minutes, and then left at room temperature (~ 20 °C). Patterns calculated based on the SCXRD structures of $\mathbf{\alpha\text{-}1}^{Si/C}$, $\mathbf{\beta\text{-}1}^{C/C}$ and $\mathbf{\gamma\text{-}1}^{C/C}$ are provided for reference. The predominant phase is indicated by the colour of the trace (black = α, red = β, blue = γ). The sample eventually returned to the β phase after an extended period.

# Comparison of PXRD traces of $1^{C/C}$, $1^{Si/C}$ and $1^{Si/Si}$

The PXRD traces of **$1^{C/C}$**, **$1^{Si/C}$** and **$1^{Si/Si}$** at 30 °C, 50 °C and 100 °C, *i.e.* the α, β and γ phases are compared in Figure S33. As can be seen, the traces for each phase are almost identical for each framework, confirming their isoreticular nature.

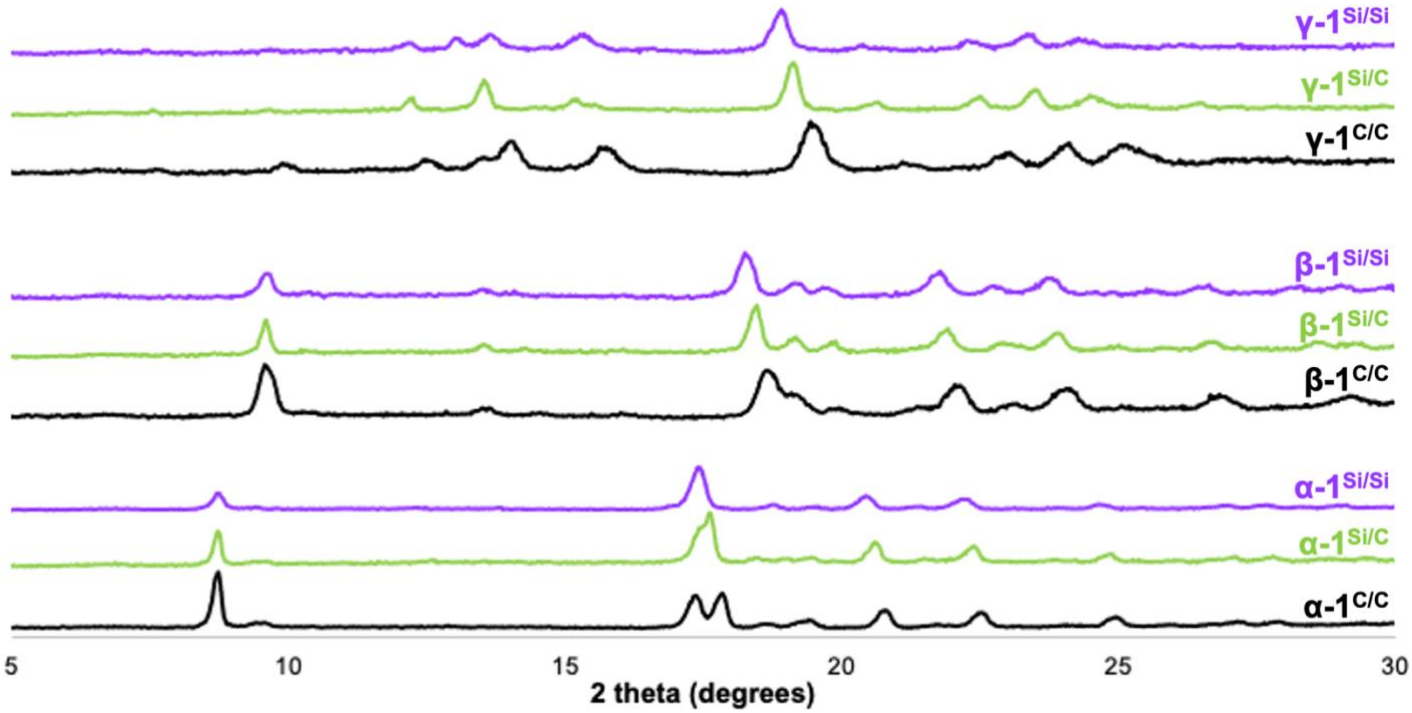


**Figure S33.** Comparison of the PXRD traces of the α, β and γ phases of **$1^{C/C}$**, **$1^{Si/C}$** and **$1^{Si/Si}$**.

# Gas sorption measurements

Gas sorption of **α-1$^{C/C}$**, **α-1$^{Si/C}$** and **α-1$^{Si/Si}$** was studied using a Micrometrics 3Flex Surface Characterization Analyzer. Samples of all frameworks were activated under dynamic vacuum at 120 °C. The sorption of $H_2$, $CO_2$ and $N_2$ by **α-1$^{C/C}$** was studied, as well as the sorption of $N_2$ by **α-1$^{Si/C}$** and **α-1$^{Si/Si}$**. In no cases was any sorption observed. PXRD studies after the sorption experiments showed that all frameworks had been converted to the β-phase during this process, which is consistent with dehydration of the α-phase under vacuum/heating giving the γ-phase and then opening to air giving the β-phase. This was investigated further by activating samples inside glass capillaries, and then flame sealing the capillaries while still under vacuum. The samples under vacuum gave PXRD traces consistent with the γ-phase. Opening the capillaries to the air resulted in slow conversion to the β-phase.

If samples of **α-1$^{C/C}$** were first solvent-exchanged with either methanol or dichloromethane before activation under vacuum, no gas uptake was observed and the framework still has the β-phase after attempted measurements and then opening to air.

# Vibrational analysis

## *Methodology*

**Infrared spectroscopy:** IR spectroscopy was carried out on **α-1$^{C/C}$** and **β-1$^{C/C}$** materials at the Terahertz and Far-Infrared beamline at the Australian Synchrotron, where an attenuated total reflection (ATR) system (Pike Technologies GladiATR) was interfaced with the beamline FTIR spectrometer (Bruker IFS125). For ATR analysis, *ca.* 1 mg quantities of sample were placed directly on a monolithic diamond prism surface with an anvil tip pressure of *ca.* 10,000 psi, under a nitrogen atmosphere and at room temperature. Far-IR photons (30–650 $cm^{-1}$) were provided by synchrotron edge radiation, separated by a 6 μm Mylar multilayer beamsplitter, and collected by a liquid-He cooled bolometer detector. The corresponding mid-IR photons (500–4000 $cm^{-1}$) were provided by a Globar (SiC) thermal light source, separated by a KBr beamsplitter, and collected by a liquid-$N_2$ cooled mid-band mercury-cadmium-telluride (MCT-B) detector. Spectrum acquisition of both regions was recorded at 4 $cm^{-1}$ resolution and averaged over 100 individual scans using OPUS version 7.2 software.[22] Post processing of retrieved spectra, including baseline correction and peak-picking, was performed using Spectragryph version 1.2.15 software.[23] Owing to the unknown index of refraction for these frameworks, no ATR corrections were performed.

**Periodic DFT:** Periodic Density Functional Theory (p-DFT) was used for the geometry optimisation and frequency analysis of the hydrogen-bonded systems using the CRYSTAL17 (C17) package;[24] applying the same protocols used by our workgroup to calculate harmonic vibrational frequencies for metal organic frameworks [25] and for hydrogen-bonded networks involving carboxyl dimer synthons.[26] This approach has resulted in synthetic IR spectra of sufficient accuracy to assign features derived from low-frequency intermolecular lattice and intramolecular torsion vibrations. These vibrational motions are prevalent in HOF systems but are otherwise difficult to model using non-periodic descriptions. Therefore, the B3LYP hybrid functional and the modified 6-311G(d), triple-ζ quality basis set[27] is employed for the periodic electronic structure calculations; augmented with D3(BJ) three-body dispersion terms (with Becke-Johnson dampening) for improved accuracy in the description of van der Waal interactions.[28,29] Total electronic energy convergence was satisfied to $10^{-8}$ au. Threshold RMS for the gradient and displacement was set to $3.0 \times 10^{-5}$ au and $1.2 \times 10^{-4}$ au, respectively, for the calculation of harmonic frequencies.

Starting geometries for the C17 input script – describing the unit cell lattice parameters, space group symmetry, and fractional atomic coordinates – were directly transcribed from the crystallography data files (CIFs) compiled for **α-1$^{C/C}$** and **β-1$^{C/C}$**. For these three-dimensional frameworks, the high space group symmetry expedites the convergence of SCF energy and structure optimization procedures where C17 optimized geometries of all systems were confirmed as valid by comparison to their respective empirical structures. However, frequency calculations for these *hydrated* systems were deemed unviable, as the treatment of the absorbed water network required excessive resources to complete. Therefore, geometry re-optimization and subsequent frequency calculations were only completed for **α-1$^{C/C}$**, where the simulated spectrum of the host HOF system (*with adsorbed water guest network removed*) assisted in assigning prominent HOF adsorption features. Here, frequency calculations at the harmonic approximation level yielded these vibrational frequencies and peak intensities (calculated through the Berry phase approach), before conversion to simulated IR spectra.

## *Far-infrared region*

Owing to their highly crystalline structures, the synchrotron far-IR spectra of **α-1**$^{C/C}$ and **β-1**$^{C/C}$ are well resolved, with both systems displaying a series of clearly defined absorption bands throughout the low frequency region (Figure S34). At frequencies higher than 400 $cm^{-1}$, vibrational features associated with low frequency intramolecular motions of the carboxylate and amidinium tectons can be assigned by p-DFT; specifically to amidinium and aromatic deformation modes (Figure S35 c–d). The peak positions and intensities of these intramolecular modes are consistent between **α-1**$^{C/C}$ and **β-1**$^{C/C}$**,** as expected for HOFs with identical subunit components, however, the p-DFT prediction of the relative intensities of these features is poor beyond the most intense peak in the region located at 440 $cm^{-1}$.

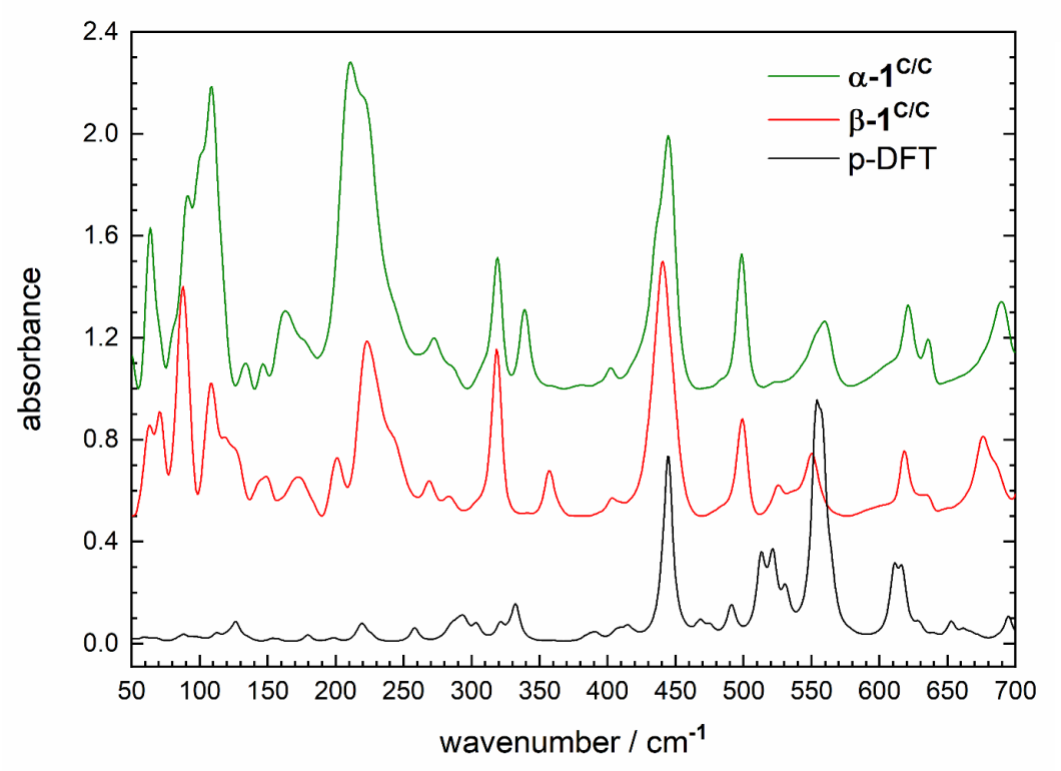


**Figure S34.** The p-DFT simulated spectra for **α-1**$^{C/C}$ (calculated from solvent-removed structure: black) compared to the synchrotron far-IR spectrum of **β-1**$^{C/C}$ (red) and **α-1**$^{C/C}$ (green). A frequency scaling factor of 0.955 has been applied for the B3LYP-D3/6-311G(d) level-of-theory in the far-IR region.

**Table S2:** Experimental far-IR frequencies for **α-1$^{C/C}$** and **β-1$^{C/C}$**, and p-DFT calculated frequencies for the solvent-removed **α-1$^{C/C}$** structure. Vibrational assignments from visualisation of mode eigenvectors.

| **α-1$^{C/C}$** | **β-1$^{C/C}$** | **p-DFT** | **Assignment** [a] |
|---|---|---|---|
| 64 | 63/71 | | |
| 109 (91sh) | 88/108 | | $H_2O$ network: donor torsion [30] |
| | | 126 | $T_d$ hindered rotation |
| 163 | 173 | | $H_2O$ network: acceptor twist [30] |
| 211 | 223 (201sh) | 218 | $T_d$ hindered rotation/deformation |
| 272 | 269 | | $H_2O$ network: in-plane shear [30] |
| | | 292 | ip phenyl hindered rotation |
| 319 | 319 | 320/332 | ip phenyl hindered rotation |
| 339 | 357 | | |
| 445 | 440 | 444 | oop amidinium deformation |
| 499 | 499 | 491 | oop amidinium deformation |
| | | 513/522 | oop phenyl hindered rotation |
| 559 | 526/550 | 554 | oop amidinium inversion |
| 621/636 | 618/634 | 611/616 | ip amidinium deformation |
| 690 | 676 | 694 | ip phenyl deformation (breathing) |

[a] $T_d$: tetrahedral; ip: in-plane; oop: out-of-plane.

At lower frequency, large amplitude distortion motions about the central tetrahedral ($T_d$) cores of the subunits are observed – often coupled to the hindered rotation of in-plane aromatic modes (Figure S35 a–b) – however, the relative intensities of these bands are predicted to be weak. This is compared to the most intense peaks in the low-frequency region that are not identified by p-DFT modelling. It is then proposed that the prominent bands between 50 and 300 $cm^{-1}$ arise from the adsorbed water network; specifically from vibrational modes associated with hydrogen-bonding donor and acceptor collective motions.[31] Such absorption features have been previously identified in far-IR measurements of water adsorbed in zeolites,[32] where expansive networks in large pore cavities result in broad, composite IR profiles. In contrast, the HOF-bound water networks in Figure S34 display rather narrow peaks that are comparable to small water clusters isolated in inert matrices;[30] where the hydrogen-bonding arrangement is well defined. Therefore the sharp far-IR features of **α-1$^{C/C}$** and **β-1$^{C/C}$** confirm the presence of highly ordered water networks residing in the small channel geometries, which are constrained through coordination to carboxylate and amidinium groups lining the channel space; corroborating the structural findings. Note also that the intensity of the ~ 90–110 and 270 $cm^{-1}$ band systems are significantly more intense for **α-1$^{C/C}$** compared to **β-1$^{C/C}$**, which is consistent with the higher water quantity of this framework.

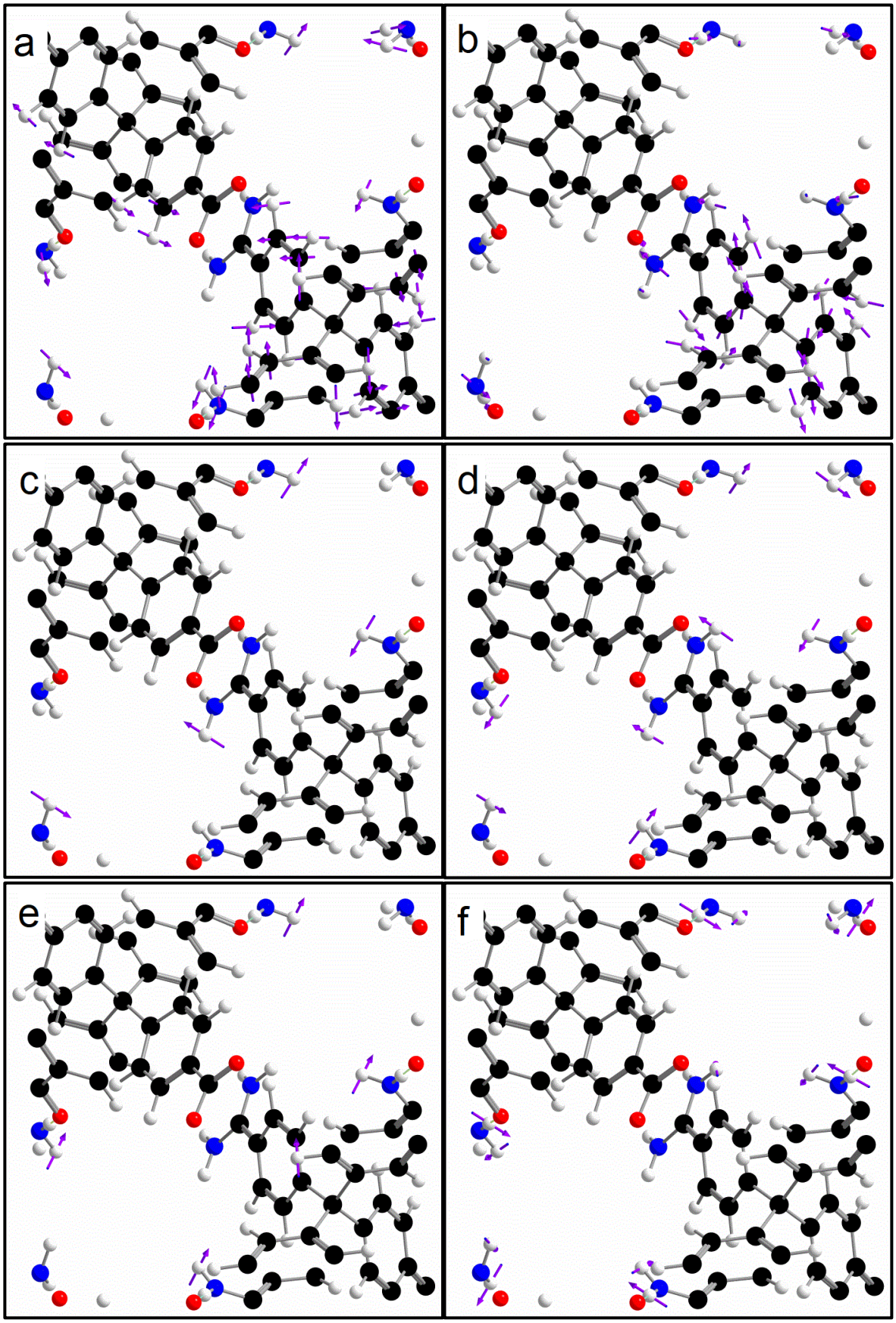


**Figure S35.** p-DFT eigenvectors (B3LYP-D3/6-311G(d)) for the most intense far-IR vibrational modes predicted for the solvent-removed **α-1**$^{C/C}$ structure; a: 126, b: 292, c: 444, d: 522, e: 554, and f: 616 cm$^{-1}$.

## *Mid-infrared region*

Information regarding the bonding and host-guest properties of the **β-1$^{C/C}$** system (Figure S36) is more difficult to discern in the mid-IR due to the high density of strong intramolecular vibration features in the region (Table S3). Below 2000 cm$^{-1}$, a number of aromatic deformation modes, some coupled to out-of-plane amidinium modes, populate the "fingerprint" region. However, these absorption bands are expected to be non-diagnostic for the class of charge-assisted hydrogen-bonded HOFs measured herein. Above 2000 cm$^{-1}$, a broad continuum of bands of carboxylate and amidinium stretching modes directly associated with the hydrogen-bonding interactions of **β-1$^{C/C}$** are identified. Here, periodic-DFT predicts the most intense IR peaks to reside at discrete frequencies from the ideal, totally symmetric geometry (where all hydrogen bonding is perfectly aligned and of uniform distance). However, in the real systems a distribution of hydrogen bonding arrangements exist to make up the frameworks, which instead sees the donor and acceptor N–H stretching modes form a continuum spanning 2000–3500 cm$^{-1}$ where only limited sub-structure may be identified due to isolated C–H and sideways (or "free") N–H group modes. Note that the prevalence of the $H_2O$ network also contributes to the high frequency composite feature in the experiment spectra via both O–H stretching motions (not observed in the solventless p-DFT simulation). It is clear that hydrogen bonding affects all stretching features due to the significant red-shift in observed frequency position from the corresponding theoretical position calculated in the absence of the hydration network. The presence of the hydration network in **β-1$^{C/C}$** is also confirmed experimentally with the $H_2O$ libration feature between 650 and 1000 cm$^{-1}$, an IR band associated with condensed-phase water.[31] Note that here we identify significant substructure within the $H_2O$ libration profile; a band that usually presents as a broad and convolved feature in extended water systems. This further supports that the water molecules within the **β-1$^{C/C}$** unit cell channel cavity are well constrained by host–guest hydrogen bonding interactions to generate a highly ordered hydration network.

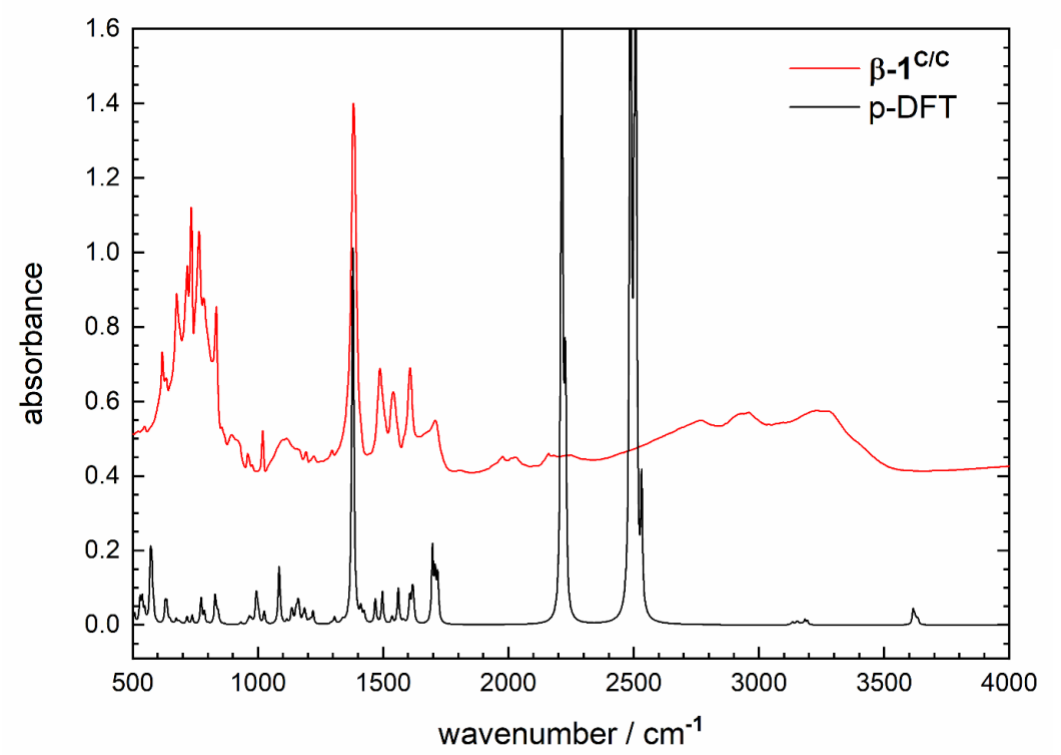


**Figure S36.** The p-DFT simulated spectra for **α-1$^{C/C}$** (calculated from solvent-removed structure: black) compared to the synchrotron mid-IR spectrum of **β-1$^{C/C}$** (red). A frequency scaling factor of 0.985 has been applied for the B3LYP-D3/6-311G(d) level-of-theory in the mid-IR region.

**Table S3:** Experimental mid-IR frequencies for **β-1**$^{C/C}$ compared to p-DFT calculated frequencies for the solvent-removed **α-1**$^{C/C}$ structure. Vibrational assignments from visualisation of mode eigenvectors.

| **β-1**$^{C/C}$ | **p-DFT** | **Assignment** [a] |
|---|---|---|
| 676 | | $H_2O$ network: libration [31] |
| 717/732 | | $H_2O$ network: libration [31] |
| 764 | 773 | oop aromatic deformation |
| 832 | 831 | oop aromatic deformation |
| 895 | | $H_2O$ network: libration [31] |
| 960 | | $H_2O$ network: libration [31] |
| 1018 | 994 | HOF H-bonding: oop amidinium NH stretch / oop aromatic C–H bend |
| 1114 | 1084 | oop amidinium bend / oop C–H bend |
| 1191 | 1162/1185 | ip asymmetric amidinium $NH_2$ bend |
| 1295 | 1305 | ip aromatic deformation |
| 1382 | 1379 | ip symmetric carboxylate COO bend |
| 1487 | 1469/1496 | ip asymmetric amidinium $NH_2$ bend / ip aromatic C–H bend |
| 1539 | 1558 | ip aromatic deformation |
| 1607 | 1613 | ip symmetric amidinium $NH_2$ bend / ip aromatic deformation |
| 1707 | 1698 | ip symmetric amidinium $NH_2$ bend |
| 2000 (br) | 2220 | HOF H-bonding: ip amidinium N–H stretch |
| 2200 (br) | 2490 | HOF H-bonding: ip amidinium N–H stretch |
| 2768 | | $H_2O$ network O–H stretch [31] |
| 2959 | | $H_2O$ network O–H stretch [31] |
| 3039 | 3180 | aromatic C–H stretch |
| 3271 | 3620 | “sideways” or “free” amidinium N–H stretch |

[a] ip: in-plane; oop: out-of-plane.

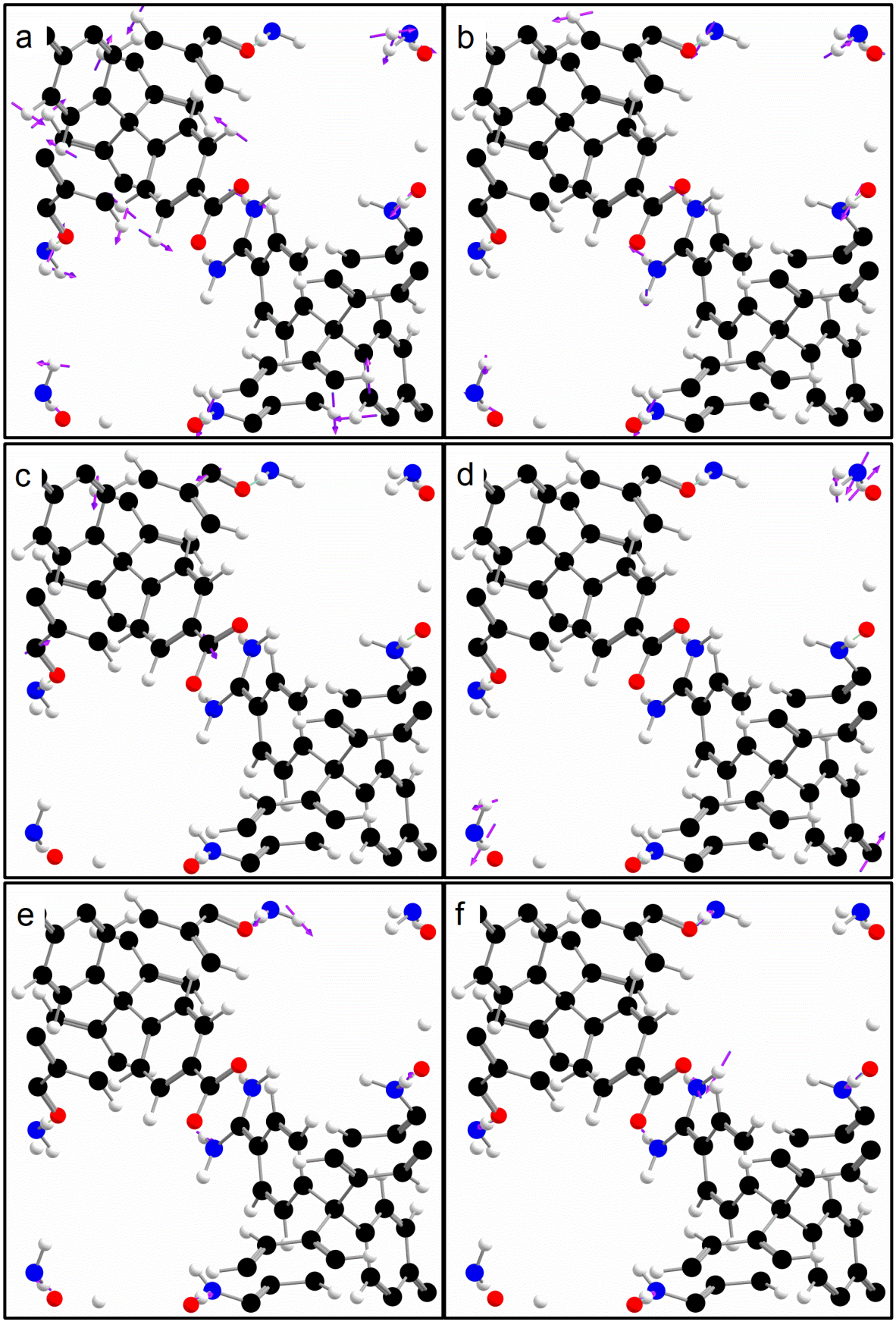


**Figure S37:** p-DFT eigenvectors (B3LYP-D3/6-311G(d)) for the most intense mid-IR vibrational modes predicted for the solvent-removed **α-1**$^{C/C}$ structure; a: 994, b: 1084, c: 1379, d: 1698, e: 2220, and f: 2490 cm$^{-1}$.

# Calculated surface areas

Accessible surface areas were calculated from the crystal structures of **α-1$^{C/C}$** (at 100 K) and **β-1$^{C/C}$** using Zeo++.[33] Solvent molecules and disorder were removed from the structures before calculations. A probe radius of 1.82 Å was used for nitrogen accessible surface areas, and 1.325 Å for water accessible surface areas and these values are presented in Table S4.

**Table S4.** Calculated accessible surface areas of **α-1$^{C/C}$** and **β-1$^{C/C}$** calculated using Zeo++.[33]

| Framework | $H_2O$-accessible surface area ($m^2\ g^{-1}$) | $N_2$-accessible surface area ($m^2\ g^{-1}$) |
|---|---|---|
| **α-1$^{C/C}$** [a] | 1330 | 810 |
| **β-1$^{C/C}$** | 740 | 0 [b] |

[a] Values calculated using a previously-reported lower quality X-ray crystal structure[10] of **α-1$^{C/C}$**, which was refined in a different space group (see SCXRD section of the Supporting Information) gave slightly lower values (1050 and 640 $m^2\ g^{-1}$ for $H_2O$ and $N_2$, respectively). [b] A non-accessible surface area of 160 $m^2\ g^{-1}$ is present.

Accessible surface areas for **α-1$^{C/C}$** and **β-1$^{C/C}$** were calculated for a range of probe radii (Figure S38). This shows that **β-1$^{C/C}$** becomes inaccessible to molecules with a probe radius greater than ~ 1.7 Å. Indeed, calculations indicate that the largest radius of a sphere that can diffuse through the frameworks is 2.36 Å for **α-1$^{C/C}$** and 1.70 Å for **β-1$^{C/C}$** (kinetic radii[34] are 1.325, 1.445, 1.65 and 1.82 Å for $H_2O$, $H_2$, $CO_2$ and $N_2$, respectively). We note that the dramatic phase change that occurs on $H_2O$ sorption means that gas sorption is not simply a case of a molecule fitting within a channel, although it seems probable that the ability of water to diffuse through the channels as **β-1$^{C/C}$** is being formed aids the transition. The output files and python code for running and analysing data using Zeo++ are available at: https://github.com/andrewtarzia/citable_data/tree/master/boer_2022.

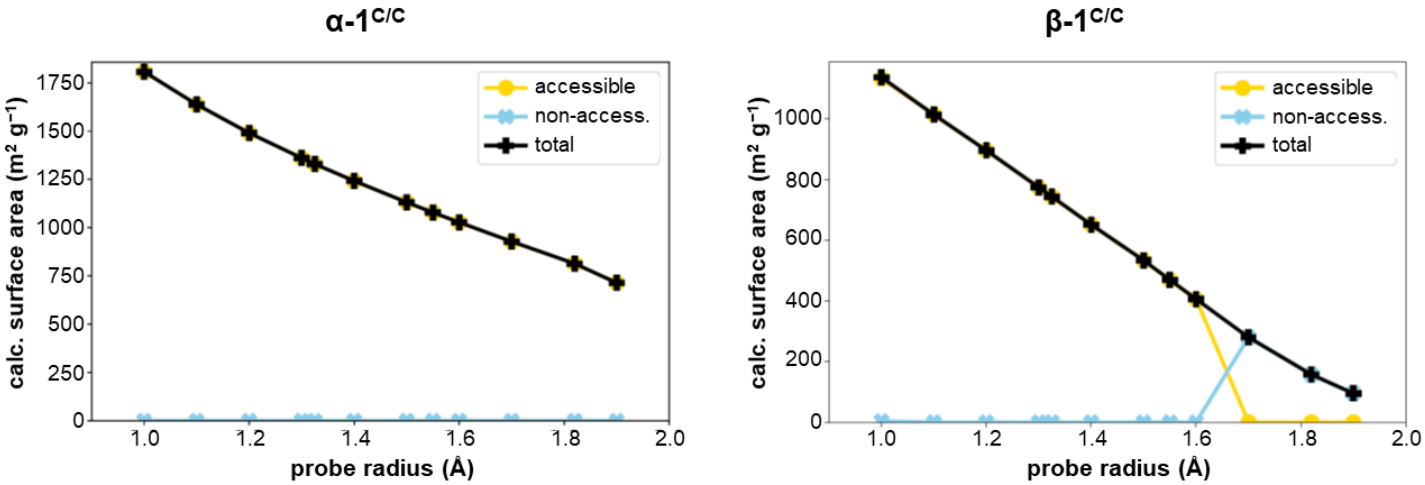


**Figure S38.** Calculated accessible, non-accessible and total (accessible + non-accessible) surface areas of **α-1$^{C/C}$** and **β-1$^{C/C}$** calculated using Zeo++[33] for various probe radii.

# References


1. H. E. Gottlieb, V. Kotlyar, A. Nudelman, *J. Org. Chem.* **1997**, *62*, 7512-7515.
2. We have found Muller and Brase's synthesis of tetra(bromophenyl)methane and tetraphenylmethane to be very convenient: O. Plietzsch, C. I. Schilling, M. Tolev, M. Nieger, C. Richert, T. Muller, S. Brase, *Org. Biomol*. *Chem.* **2009**, *7*, 4734-4743.
3. AKSci and Combi-Blocks sell 10 g of this compound for approximately US$200. Other suppliers appear to be significantly more expensive.
4. S. A. Boer, L.-J. Yu, T. L. Genet, K. Low, D. A. Cullen, M. G. Gardiner, M. L. Coote, N. G. White, *Chem. Eur. J.* **2021**, *27*, 1768-1776.
5. C. Ennis, S. A. Boer, D. Appadoo, N. G. White, *Phys. Chem. Chem. Phys.* **2022**, DOI: 10.1039/d2cp00796g.
6. M. Morshedi, N. G. White, *CrystEngComm*, **2017**, *19*, 2367-2371.
7. M. Morshedi, M. Thomas, A. Tarzia, C. J. Doonan, N. G. White, *Chem. Sci.* **2017**, *8*, 3019-3025.
8. M. Grimm, B. Kirste, H. Kurreck, *Angew. Chem. Int. Ed.* **1986**, *25*, 1097-1098.
9. H. Qian, S. Li, J. Zheng, S. Zhang, *Langmuir*, **2012**, *28*, 17803-17810.
10. S. A. Boer, M. Morshedi, A. Tarzia, C. J. Doonan, N. G. White, *Chem. Eur. J.* **2019**, *25*, 10006-10012.
11. L.-J. Yu, D. A. Cullen, M. Morshedi, M. L. Coote, N. G. White, *J. Org. Chem.* **2021**, *86*, 13762-13767.
12. D. Aragao, J. Aishima, H. Cherukuvada, R. Clarken, M. Clift, N. P. Cowieson, D. J. Ericsson, C. L. Gee, S. Macedo, N. Mudie, S. Panjikar, J. R. Price, A. Riboldi-Tunnicliffe, R. Rostan, R. Williamson, T. T. Caradoc-Davies, *J. Synchotron Radiat.* **2018**, *25*, 885-891.
13. N. P. Cowieson, D. Aragao, M. Clift, D. J. Ericsson, C. H. Gee, Stephen J., N. Mudie, S. Panjikar, J. R. Price, A. Riboldi-Tunnicliffe, R. Williamson, T. Caradoc-Davies, *J. Synchotron Radiat.* **2015**, *22*, 187--190.
14. W. Kabsch, *J. Appl. Crystallogr.* **1993**, *26*, 795-800.
15. *CrysAlis Pro*, Oxford Diffraction, **2011**.
16. L. Palatinus, G. Chapuis, *J. Appl. Crystallogr.* **2007**, *40*, 786-790.
17. G. Sheldrick, *Acta Crystallogr.* 2015, **A71**, 3-8.
18. P. W. Betteridge, J. R. Carruthers, R. I. Cooper, K. Prout, D. J. Watkin, *J. Appl. Crystallogr.* **2003**, *36*, 1487.
19. R. I. Cooper, A. L. Thompson, D. J. Watkin, *J. Appl. Crystallogr.* **2010**, *43*, 1100-1107.
20. A. L. Spek, *Acta Crystallogr.* **2015**, *C71*, 9-18.
21. D. A. Cullen, M. G. Gardiner, N. G. White, *Chem. Commun.* **2019**, *55*, 12020-12023.
22. *OPUS 7.2*, Bruker Optik GmbH, **2012**.
23. F. Menges, *Spectragryph 1.2.15*, **2019**.
24. R. Dovesi, V. Saunders, C. Roetti, R. Orlando, C. Zicovich-Wilson, F. Pascale, B. Civalleri, K. Doll, N. Harrison, I. Bush, *CRYSTAL17*, **2017**.
25. C. Ennis, A. C. Tay, J. L. Falconer, S. Lee, C. J. Meledandri, *J. Phys. Chem. C* **2021**, *125*, 20426-20438.
26. E. M. Lippitt, C. Ennis, S. C. Moratti, L. R. Hanton, *Cryst. Growth Des.* **2020**, *20*, 7805-7821.
27. J. Heyd, J. E. Peralta, G. E. Scuseria, R. L. Martin, *J. Chem. Phys.* **2005**, *123*, 174101.
28. S. Grimme, J. Antony, S. Ehrlich and H. Krieg, *J. Chem. Phys.* **2010**, *132*, 154104.
29. S. Grimme, S. Ehrlich, L. Goerigk, *J. Comput. Chem.* **2011**, *32*, 1456-1465.
30. J. Ceponkus, B. Nelander, *J. Phys. Chem. A* **2004**, *108*, 6499-6502.
31. J.-B. Brubach, A. Mermet, A. Filabozzi, A. Gerschel, P. Roy, *J. Chem. Phys.* **2005**, *122*, 184509.
32. B. Hunger, S. Matysik, M. Heuchel, E. Geidel H. Toufar, *J. Therm. Anal. Calorim.* **1997**, *49*, 553-565.
33. T. F. Willems, C. H. Rycroft, M. Kazi, J. C. Meza, M. Haranczyk, *Microporous Mesoporous Mater.* **2012**, *149*, 134-141.
34. C. Scholes, S. Kentish, G. Stevens, *Recent Pat. Chem. Eng.*, **2008**, *1*, 52-66.